Effects of Fault Dip and Slip Rake Angles on Near-Source Ground Motions: Why the 1999 *M* 7.6 Chi-Chi, Taiwan, Earthquake Was Relatively Mild

by Brad T. Aagaard, John F. Hall, and Thomas H. Heaton

Abstract We study how the fault dip and slip rake angles affect near-source ground velocities and displacements as faulting transitions from strike-slip motion on a vertical fault to thrust motion on a shallow-dipping fault. Ground motions are computed for five fault geometries with different combinations of fault dip and rake angles and common values for the fault area and the average slip. The nature of the shear-wave directivity is the key factor in determining the size and distribution of the peak velocities and displacements. Strong shear-wave directivity requires that (1) the observer is located in the direction of rupture propagation and (2) the rupture propagates parallel to the direction of the fault slip vector. We show that the ground motions in the Chi-Chi earthquake were relatively mild because the rupture propagated perpendicular to the slip vector; that is, the rupture propagated in the direction of a node in the shear-wave radiation pattern. In our simulations with a shallow hypocenter, the maximum peak-to-peak horizontal velocities exceed $1.5\,\mathrm{m/s}$ over an area of only $200\,\mathrm{km}^2$ for the 30 degree dipping fault (Chi-Chi), whereas for the 60 and 75 degree dipping faults this velocity is exceeded over an area of $2700\mathrm{km}^2$. These simulations suggest that the area subjected to large long-period ground motions in the 1999 Chi-Chi earthquake in Taiwan was much smaller than what would be expected for other events of the same size with different styles of faulting or a deeper hypocenter.

Introduction

In the past decade several earthquakes near large urban areas have caused considerable damage, including the 1994 Northridge, California, 1995 Hyogo-Ken Nanbu (Kobe), Japan, the 1999 Izmit and Duzce, Turkey, and 1999 Chi-Chi, Taiwan, earthquakes. These earthquakes and their associated ground motion records increased the awareness of the destructive capability and characteristics of near-source ground motions (e.g., see Olsen and Archuleta (1996), Somerville *et al*. (1997), Hisada *et al*. (1998), Kamae and Irikura (1998), Pitarka *et al*. (1998), Huang *et al*. (2000), Oglesby *et al*. (2000)). Two factors control the amplitude of near-source ground motions. At all locations in the near field, the directivity of the rupture affects the amplitude of the motion. Additionally, at locations very close to the fault trace, the static offset also contributes to the amplitude of the motion. This means that for events of the same size, which have similar static offsets, changes in the rupture directivity largely determine the variations in the amplitude of the near-source ground motions from one event to another. The primary factor controlling the size of the directivity effect is not simply the distance the rupture propagates but the distance the rupture propagates toward a location while it is parallel to the direction of slip. Consequently, the dimensions and the dip angle of the fault, the direction of slip (slip rake angle), and the location of the hypocenter all play critical roles in determining the character and amplitude of near-source ground motions.

Early efforts aimed at understanding near-source ground motions focused on simple numerical models (e.g., Haskell (1969), Archuleta and Frazier (1978), and Archuleta and Hartzell (1981)). More recently, some researchers have focused on specific ground motion recordings (Iwan and Chen, 1994) or damage near a surface rupture (Allen *et al*., 1998) to infer the characteristics of near-source ground motions. In addition to the modeling efforts mentioned above that attempt to explain damage in past earthquakes, three-dimensional simulations have focused on hypothetical scenarios. Olsen *et al*. (1995) and Graves (1998) examined near-source ground motions for ruptures on the San Andreas fault, and Olsen and Archuleta (1996) considered various scenarios within the Los Angeles area. Whereas these previous studies help to explain patterns of damage in particular earthquakes or what such patterns might be for some future event, they generally do not shed light on the fundamental characteristics of near-source ground motions and how these vary with changes in the seismic source parameters. Dynamic rupture models have improved our understanding of how near-source ground motions develop from the basic features of the rupture process (Olsen *et al*., 1997; Inoue and Miyatake, 1998; Oglesby *et al*., 2000; Aagaard *et al*., 2001), but only a couple of these studies (Oglesby *et al*., 2000; Aagaard *et al*., 2001) have systematically explored how the source parameters affect the near-source ground motions.

We complement these two efforts and other work (Aagaard *et al*., 2001), that used kinematic source models to systematically examine source parameters and near-source ground motions, by focusing on an event of a specific size and determining how changes in the style of faulting, in

particular the fault dip and slip rake angles, affect the near-source ground motions. We examine the distribution of shaking and the characteristics of the near-source ground motions, as well as how these change in response to variations in the fault dip and slip rake angles for two hypocenters. We consider several measures of the ground motions, including the horizontal acceleration response spectra, the area where the ground motion exceeds a given level, and the mean maximum amplitude of the motion as a function of distance from the fault. Furthermore, by selecting a parameter space that includes a scenario that approximately matches the 1999 Chi-Chi earthquake in Taiwan, we explore the role that the style of faulting played in determining the intensity of the long-period shaking in the Chi-Chi earthquake.

These long-period ground motions place the greatest demand on structures with similar fundamental periods, such as 20 story buildings (Hall *et al*., 1995). Even though ground motions at higher frequencies ($f > 1$ Hz) appear to have much less systematic variation (Heaton, 1995) and most structures have periods shorter than 1 s, ground motion intensities at longer periods appear to correlate well with measures of structure damage. Boatwright *et al*. (2001) noted that the distribution of red tagged buildings following the 1994 Northridge earthquake closely resembled the distributions of peak ground velocity for periods around 1.5 s. Similarly, Wald *et al*. (1999) developed a linear regression between peak velocity and modified Mercalli intensity for eight California earthquakes. Thus, although the bandwidth of the simulations in this study is restricted to periods of 2 s and longer and are most applicable to structures with similar periods, the distributions of shaking likely also correlate with damage of structures at shorter periods. Furthermore, variations in the shaking across the scenarios would indicate similar changes to the distribution of damage.

Earthquake Scenarios

We compute the near-source ground motions for two hypocenters for each of five different pairs of fault dip and slip rake angles. We also select a realistic fault length-to-width ratio for each dip angle. The scenarios vary from a pure strike-slip rupture on a long, narrow fault to a pure thrust rupture on a significantly shorter and wider fault.

Methodology

We follow the general methodology of our previous work involving simulations of near-source ground motions, so this section contains only a brief summary of the methods used in the earthquake simulations. Aagaard (1999) and Aagaard *et al*. (2001) provide detailed discussions of the methodology. This study improves upon our previous characterizations of the seismic source; in particular, the length scales of the spatial heterogeneity in the final slip are compatible with those found in kinematic source inversions, and we allow the rupture speed to vary as a function of the direction of propagation relative to the direction of slip.

We discretize the three-dimensional domain using linear tetrahedral finite elements. This transforms the three-dimensional dynamic elasticity equation,

$$\lambda u_{k,kj}\delta_{ij} + \mu(u_{i,jj} + u_{j,ij}) = \rho\ddot{u}_i \qquad (1)$$

into a matrix differential equation,

$$[M]\{\ddot{u}(t)\} + [C]\{\dot{u}(t)\} + [K]\{u(t)\} = \{F(t)\}, \qquad (2)$$

where $[M]$ denotes the mass matrix, $[C]$ denotes the damping matrix, $[K]$ denotes the stiffness matrix, $\{F(t)\}$ denotes the force vector at time t, and $\{u(t)\}$ denotes the displacement vector at time t. Our discretization of the finite-element model limits the simulation to wave propagation for waves with periods of 2.0 s and longer.

Anelastic attenuation is not included because it has little effect on long-period near-source ground motions, so the only contribution to the damping matrix comes from the absorbing boundaries on the lateral sides and bottom of the domain. These absorbing boundaries prevent waves from reflecting off the truncated sides of the domain and contaminating the solution.

We model the earthquake by creating dislocations in the finite-element model that mimic the slip on a fault. In the scenarios discussed here, we specify the slip time history at each point on the fault, where the time history follows the integral of Brune's far field time function with the final slip and peak slip rate as parameters.

Simulation Domain

In each of the scenarios, the domain is 160 km long, 80 km wide, and 40 km deep as shown in figure 1. The material properties vary only as a function of depth as illustrated in figure 2. This set of material properties represents the average variations in Taiwan and corresponds to the variation in a region without a deep sedimentary basin (Ma *et al*., 1996; Ma *et al*., 2001).

Earthquake Source Parameters

Table 1 gives the five pairs of fault dip and slip rake angles along with the fault lengths and widths for the different fault geometries. For the five fault geometries we chose fault dip angles uniformly distributed between 90 and 30 degrees with rake angles uniformly distributed between 0 and 90 degrees. Similarly, the lengths of the faults decrease linearly from 120 km long to 80 km long while maintaining an area of 2400 km^2. The 80 km long and 30 km wide fault which has a dip angle of 30 degrees roughly matches the geometry of the 1999 Chi-Chi earthquake in Taiwan. Inversions for the source characteristics indicate this earthquake had a rupture length of between 80 km and 100 km, a rupture width of between 30 m and 40 km, and a dip angle of 20 degrees to 30 degrees (Huang *et al*., 2000; Ma *et al*., 2000; Johnson *et al*., 2001; Ji *et al*., 2001). The length to width ratios and slip rake angles all fall within the ranges of realistic values for the five fault dip angles.

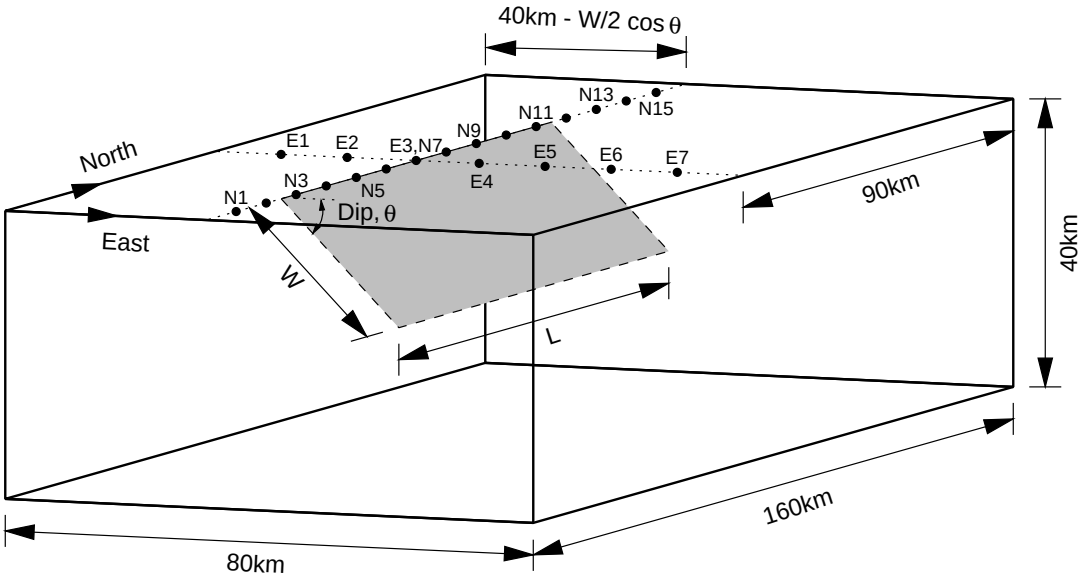

Figure 1. Geometry of the simulation domain. The fault has a dip angle of θ, a length of L, and a width of W. The center of the fault lies 10 km south of the center of the domain. The dotted line running east-west sits above the center of the fault, whereas the dotted line running north-south intersects the fault trace. The filled circles along these two dotted lines identify sites (N1 through N15 and E1 through E7) used in subsequent sections. The nominal spacing between sites is 10 km with those along the fault trace sitting on the east side of the fault (hanging wall).

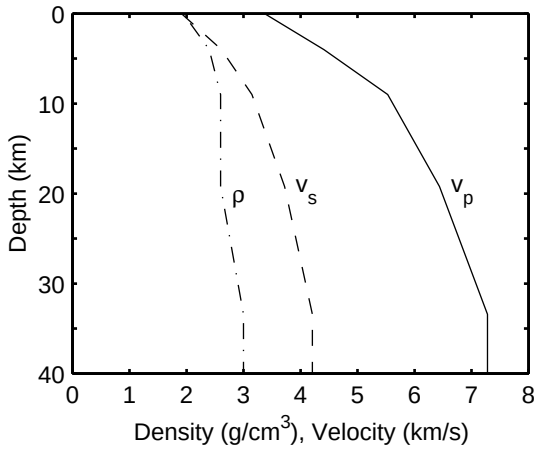

Figure 2. Dilatational wave speed (v_p), shear wave speed (v_s), and mass density (ρ) as a function of depth.

Table 1

Seismic source parameters for each pair of fault dip and slip rake angles. The style of faulting smoothly transitions from pure strike-slip motion on a long, narrow fault to pure thrust motion on a much shorter, wider fault. The rupture speed is set relative to the local shear wave speed, v_s.

Dip Angle (deg)	Rake Angle (deg)	Fault Length (km)	Fault Width (km)	Average Slip (m)	Peak Slip Rate (m/s)	Rupture Speed (%v_s)
90	0.0	120	20	2.9	2.0	85% parallel to slip 68% perp. to slip
75	22.5	110	22			
60	45.0	100	24			
45	67.5	90	27			
30	90.0	80	30			

Based on the regression relations of Wells and Coppersmith (1994) between fault geometry and average slip coupled with these fault dimensions, we chose a common average slip of 2.9 m for the scenarios. This average slip is smaller than the average slip estimated for the Chi-Chi earthquake, so our fault with a dip angle of 30 degrees and our choice of material properties has a moment magnitude of only 7.4 compared with the moment magnitude of 7.6–7.7 estimated for the Chi-Chi earthquake. For each fault the slip rake angles are uniform and remain constant during the rupture. We also use a uniform peak slip rate of 2.0 m/s in the slip time history, which, for final slips of around 3 m, gives slip durations compatible with those found in kinematic source inversions (Heaton, 1990; Somerville *et al*., 1997).

We create the distributions of slip by low-pass filtering random distributions. Starting with a uniform random distribution on a 1.0 km uniform grid (which is coarser than the node spacing in the finite-element model), we low-pass filter along the fault strike and then along the dip using a first order Butterworth filter. We also taper the slip along the buried edges of the fault. Whereas the distributions for each fault geometry all have an average slip of 2.9 m, the maximum slip ranges from 5.7 m to 7.1 m because we start with different random distributions for each fault geometry. Figure 3 shows the distribution of final slip for the fault with a dip angle of 60 degrees. Although a power-law spectral falloff would create slip distributions that better match what is found in kinematic source inversions (Somerville *et al*., 1997; Mai and Beroza, 2002), the long-period near-source ground motions are relatively insensitive to the distribution of slip (Aagaard *et al*., 2001), so that the dominant features of the ground motions do not change when using a low-pass filtered random distribution compared with a power-law filtered random distribution.

Figure 4 shows the two hypocenters we consider for each dip angle of the fault. The shallow hypocenter sits mid-depth at the southern quarter point of the fault and corresponds to a highly unilateral rupture, whereas the deep hypocenter sits 5.0 km up-dip from the bottom center of the fault and corresponds to a bilateral case with more up-dip rupture. For strike-slip faulting the ruptures propagate mostly in the mode-II direction (parallel to slip and a local maximum in shear-wave radiation pattern) for both hypocenters. On the other end of the spectrum, for pure thrust faulting and the shallow hypocenter the rupture propagates primarily in the mode-III direction (perpendicular to slip and a node in the shear-wave radiation pattern) with very little propagation in the mode-II direction; for pure thrust faulting and the deep hypocenter the amount of rupture in the mode-II direction increases significantly.

The rupture speed determines when slip begins at each point on the fault. Numerous dynamic rupture simulations (e.g., Andrews (1976), Day (1982), Madariaga *et al*. (1998), Aagaard *et al*. (2001)) indicate that ruptures propagate slightly slower in the direction perpendicular to slip (mode-III direction) compared with the direction parallel to slip (mode-II direction). Therefore, instead of an isotropic rupture speed, we independently specify the rupture speed to be 85% of the local shear wave speed in the mode-II direction (parallel to the slip direction) and 20% slower in the mode-III direction (perpendicular to the slip direction) as illustrated in figure 4.

Scenario Nomenclature

The name of each scenario corresponds to the dip angle of the fault and the location of the hypocenter. For example, Dip90Shallow refers to the scenario where the fault has a dip angle of 90 degrees and the rupture begins at the shallow hypocenter. Similarly, Dip45Deep refers to the scenario where the fault has a dip angle of 45 degrees and the rupture begins at the deep hypocenter.

Results

Overview of Rupture Behavior and Ground Motions

We begin by examining how the basic characteristics of the rupture behavior and resulting ground motions change with the fault dip and slip rake angles using data from scenario Dip90Shallow (pure strike-slip faulting with predominantly unilateral rupture). Additional results and figures can be found in Aagaard *et al*. (2002). In scenario Dip90Shallow, the rupture propagates fastest along the strike of the fault. As we vary the style of faulting across the scenarios by decreasing the dip angle of the fault and increasing the rake angle of slip so that it has a larger vertical component, the rupture speed along the strike decreases while the rupture speed up-dip increases. For the case of the fault at a dip angle of 45 degrees and a rake angle of 67.5 degrees, the fastest rupture speed occurs 22.5 degrees off the up-dip and down-dip directions. This creates asymmetry in the propagation of the rupture for the centrally located deep hypocenter.

Due to the existence of surface rupture in the layered medium, surface waves in the form of combinations of Love and Rayleigh waves dominate the long-period ground motions. As the rupture propagates in scenario Dip90Shallow, large-amplitude Love waves with amplitudes approaching 2.0 m/s form in the region where the propagation direction generally coincides with the slip direction, which in this case is north of the epicenter. The particle motion for these waves is in the east-west direction (normal to the fault). The Love wave amplitudes generally build along the length of the fault as the rupture reinforces the waves, and then begin steadily decreasing upon reaching the northern tip of the fault. The heterogeneous distribution of slip disrupts the reinforcement of the Love waves, so that the amplitudes undergo minor fluctuations as they grow.

As the dip angle of the fault decreases and the vertical component of slip increases, the rupture generates Love waves less effectively and becomes more effective at generating Rayleigh waves. The rotation of the slip direction toward the dip direction results in reinforcement of the SV

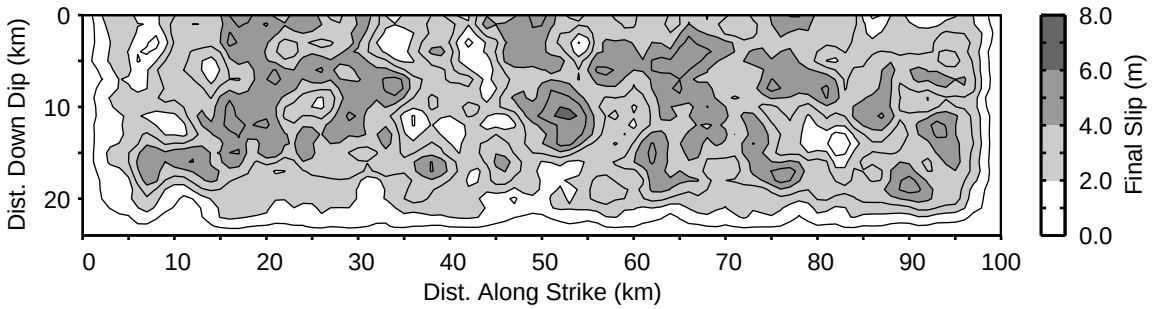

Figure 3. Distribution of final slip for the fault that has a dip angle of 60 degrees. The distribution is a low-pass filtered random distribution.

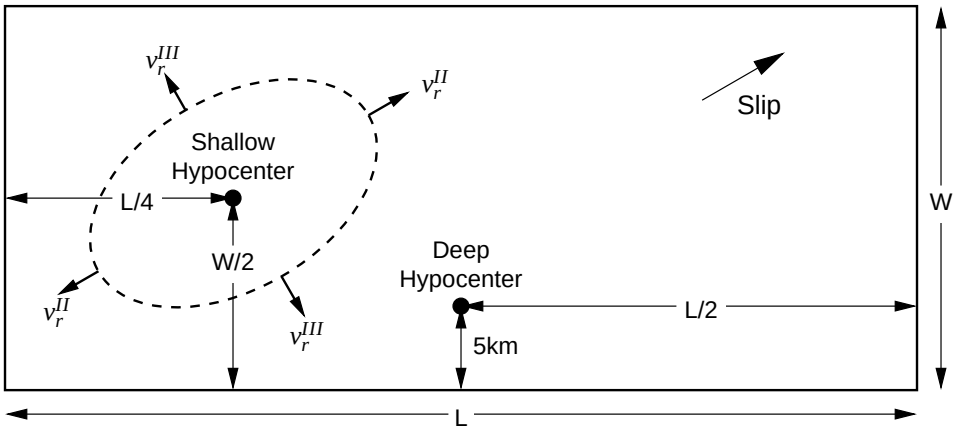

Figure 4. Relative locations of the shallow and deep hypocenters on the fault surface which has a length of L and a width of W. The shallow hypocenter lies mid-depth at a quarter point and the deep hypocenter lies midway along strike 5 km up-dip from the bottom of the fault. The shallow hypocenter corresponds to the general location of the hypocenter in the Chi-Chi earthquake. The dashed ellipse identifies the rupture front at some point in time propagating away from the shallow hypocenter and illustrates how the rupture speed is set independently in the mode-II (v_r^{II}) and mode-III (v_r^{III}) directions.

waves (shear waves with particle motion in the vertical direction) emanating from an angle of 45 degrees with respect to the slip direction. These SV waves produce Rayleigh waves as they hit the ground surface. Consequently, the largest Rayleigh waves (with amplitudes near 1.5 m/s) occur northwest of the epicenter; the particle motions are retrograde with the largest horizontal component in the northwest-southeast direction.

Maximum Displacements and Velocities

Choices for measuring the intensity of the shaking include the maximum amplitude of the motion and the maximum peak-to-peak amplitude of the motion. In practice, the greatest difference between the two occurs for the case of double-sided, symmetric displacement or velocity pulses, as shown in figure 5. A displacement ramp and the corresponding single-sided velocity pulse roughly approximate the ground motion at a location with a static offset. In this case, there is no difference between the maximum peak-to-peak amplitude and the maximum amplitude. A single-sided displacement pulse and the corresponding double-sided velocity pulse roughly approximate the ground motion at a location without a static offset and no surface waves. Whereas the maximum displacement equals the maximum peak-to-peak displacement, the maximum peak-to-peak velocity exceeds the maximum velocity by up to a factor of two. Finally, a double-sided displacement pulse and the corresponding velocity pulses roughly approximate the ground motion at a location with large amplitude surface waves and no static offset. In this case, the maximum peak-to-peak displacement and velocity amplitudes can both be up to twice the maximum amplitudes. We will use the maximum magnitude of the displacement and the maximum peak-to-peak velocity as measures of ground motion intensity because double-sided velocity pulses place a greater demand on structures than single-sided velocity pulses (Hall *et al*., 1995).

In scenario Dip90Shallow the maximum horizontal displacements and maximum peak-to-peak horizontal velocities increase along the strike of the fault north and south of the epicenter as shown in figure 6. This effect is much more pronounced north of the epicenter because the rupture extends much further in this direction compared with south of the epicenter. The amplitudes also decay rapidly with distance away from the surface trace of the fault. The maximum horizontal displacement is 2.6 m, and the maximum peak-to-peak horizontal velocity is 2.6 m/s.

As the dip of the fault decreases and the vertical component of slip increases, the pattern of shaking becomes much

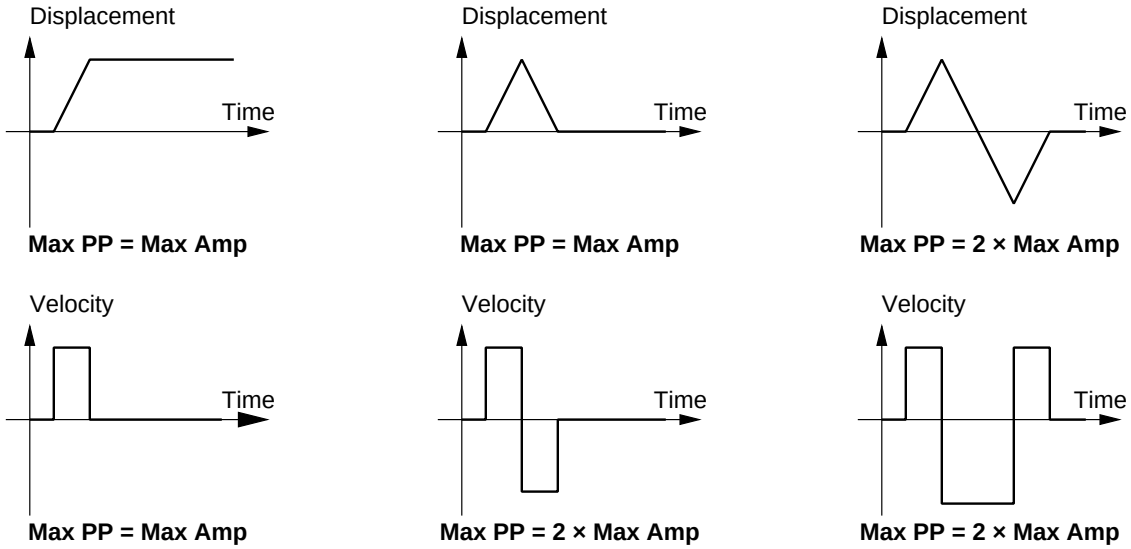

Figure 5. Illustration of how the peak-to-peak displacement and velocity amplitudes compare to the maximum amplitudes for three different types of ground motions: a displacement ramp and corresponding single-sided velocity pulse (left), a single-sided displacement pulse and corresponding double-sided velocity pulse (center), and a double-sided displacement pulse and corresponding velocity pulses (right). Except for the case of double-sided displacements, which are generally associated with surface waves, the maximum peak-to-peak displacements match the maximum displacements. On the other hand, the maximum peak-to-peak velocities exceed the maximum velocities except for the case in which there is a large static offset.

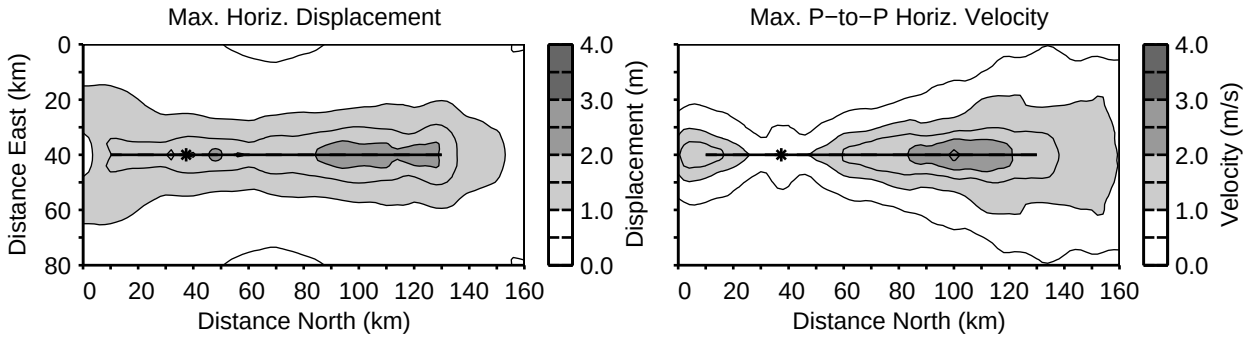

Figure 6. Maximum amplitude of the horizontal displacements and maximum peak-to-peak horizontal velocities on the ground surface for scenario Dip90Shallow. The thick solid line shows the surface trace of the fault and the asterisk identifies the epicenter. The maximum displacements and velocities generally increase along the fault away from the epicenter and then decrease steadily past the ends of the fault.

more asymmetric with two clear features: (1) the ground displacements on the hanging-wall (above the fault) increase and closely resemble the distribution of slip, and (2) the strongest shaking remains concentrated in the region with the maximum directivity. These trends are visible in figure 7, which displays the maximum displacements and maximum peak-to-peak velocities for scenario Dip60Shallow. The steep dip of the fault and the rake angle of 45 degrees lead to large Love and Rayleigh waves that propagate toward the northwest. As a result, a large region emanating off to the northwest from the northern end of the fault experiences maximum displacements exceeding 1.0 m and maximum peak-to-peak velocities exceeding 2.0 m/s.

With the shallow hypocenter, as we transition from strike-slip motion to thrust motion, the rupture continues to propagate mostly along the strike of the fault so that the rupture direction becomes less aligned with the slip direction. In other words, the rupture switches from propagating in the mode-II direction, which is a local maximum in the shear-wave radiation pattern, to propagating in the mode-III direction, which is a node in the shear-wave radiation pattern. In our limiting case where the fault dip angle is 30 degrees with pure thrust faulting, the inability of the rupture to effectively reinforce Love or Rayleigh waves leads to much smaller velocities on the ground surface (figure 8). Although the maximum velocities do reach 1.4 m/s at one location, the maximum peak-to-peak velocity is only 1.7 m/s. On the hanging wall of the fault, the maximum displacements do remain large although they are dominated by the static displacement which is consistent with equal values of 3.1 m for the maximum amplitude and the maximum peak-to-peak amplitude.

However, moving the hypocenter toward the bottom center of the fault increases the amount of mode-II rupture for the thrust motion cases. Of course, it has the opposite effect for the case of pure strike-slip motion on a vertical fault

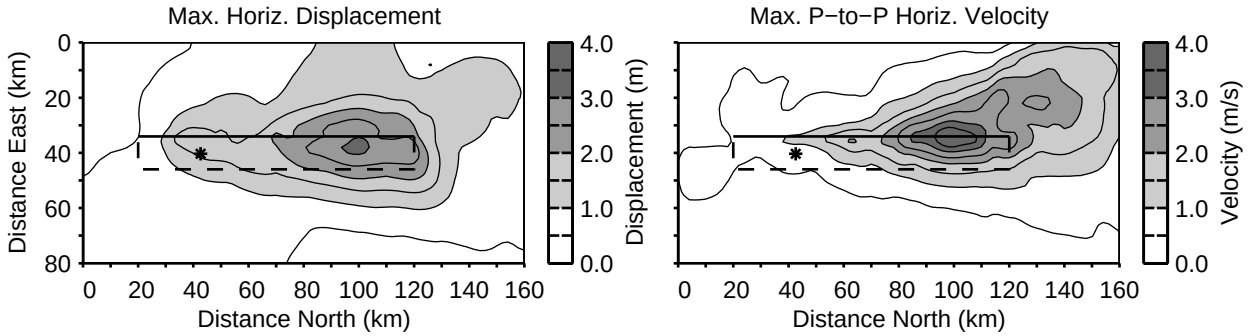

Figure 7. Maximum horizontal displacements and maximum peak-to-peak horizontal velocities on the ground surface for scenario Dip60Shallow. The thick solid line shows the surface trace of the fault, the thick dashed line indicates the surface projection of the buried edges of the fault, and the asterisk identifies the epicenter. The maximum displacements and velocities generally increase along the fault away from the epicenter with a large region of intense shaking extending to the northwest.

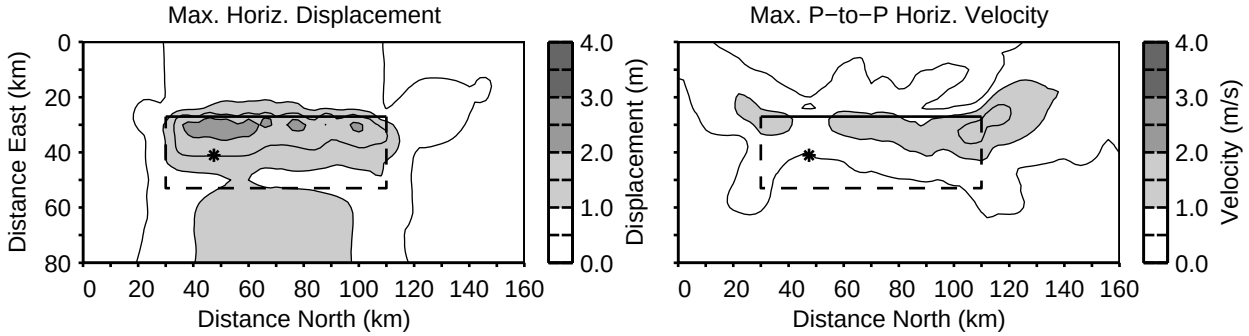

Figure 8. Maximum horizontal displacements and maximum peak-to-peak horizontal velocities on the ground surface for scenario Dip30Shallow (Chi-Chi). The thick solid line shows the surface trace of the fault, the thick dashed line indicates the surface projection of the buried edges of the fault, and the asterisk identifies the epicenter. The predominantly mode-III rupture does not efficiently reinforce the Love and Rayleigh waves, which results in much smaller ground motions relative to the other scenarios.

where the distance over which the rupture effectively reinforces waves decreases by one third. Thus, for the steeply-dipping faults with mostly horizontal slip, the ground motions decrease in most locations when the hypocenter moves to the deeper, more central location, whereas for shallow-dipping faults with a large thrust component of slip, the ground motions increase at many locations. For the 60 degree dipping fault with a slip rake angle of 45 degrees, the maximum peak-to-peak velocity is 33% smaller for the deep hypocenter compared with the shallow hypocenter. On the other hand, for the 30 degree dipping fault with a slip rake angle of 90 degrees (pure thrust), the maximum peak-to-peak velocity *increases* by 30% when the hypocenter moves from the shallow location to the deep location.

Table 2 give the maximum displacements and the maximum peak-to-peak velocities in the east-west, north-south, and vertical directions as well as the maximum in any horizontal direction for each of the ten scenarios. In all ten scenarios the ground motions are large with the maximum displacements exceeding 2.2 m and the maximum peak-to-peak velocities exceeding 1.7 m/s.

Ground Motion Time Histories

In this section we examine the velocity time histories at a set of sites located along two perpendicular lines on the ground surface (dotted lines shown in figure 1). The north-south line runs along the entire length of the domain and over the surface trace of the fault with the sites sitting on the hanging wall of the fault. The east-west line runs across the entire width of the domain perpendicular to the strike of the fault; it sits above the center of the fault. On both lines the sites lie approximately 10 km apart.

The velocity time histories for scenario Dip90Shallow, which are shown in figure 9, further illustrate the trends seen in the plots of the maximum displacements and velocities. At all of the sites, the vertical components are negligible compared with the north-south and east-west components for the pure strike-slip faulting. The slip time histories dominate the north-south components (fault parallel) along the surface trace of the fault, whereas the Love waves dominate the east-west components. The velocities along the east-west line demonstrate that the strongest motions are concentrated near the trace of the fault.

As the dip of the fault decreases and the slip rake angle increases, the amplitudes of the Love waves decrease and the amplitudes of the Rayleigh waves increase. This corresponds to a decrease in motion in the east-west direction and an increase in motion in the north-south and vertical directions. For scenario Dip60Shallow (figure 10) the amplitudes of the three components are relatively equal, because the motions contain large-amplitude Love and Rayleigh waves.

Table 2

Maximum displacements and maximum peak-to-peak velocities in the east-west, north-south, horizontal, and vertical directions for each scenario.

Scenario	Max. Disp.				Max. P-to-P Velocity			
	EW (m)	NS (m)	Horiz. (m)	Vert. (m)	EW (m/s)	NS (m/s)	Horiz. (m/s)	Vert. (m/s)
Dip90Shallow	2.0	2.6	2.6	0.76	2.6	1.0	2.6	0.80
Dip90Deep	1.8	2.6	2.6	0.74	2.0	1.1	2.0	0.72
Dip75Shallow	3.1	3.1	3.3	1.4	3.6	1.5	3.7	1.2
Dip75Deep	2.1	3.1	3.1	1.3	2.5	1.3	2.8	1.2
Dip60Shallow	3.1	2.8	3.2	2.9	3.9	2.4	4.2	3.0
Dip60Deep	2.2	2.8	2.8	2.5	2.4	2.2	2.8	2.2
Dip45Shallow	2.1	2.2	2.2	3.5	2.0	2.5	2.7	3.9
Dip45Deep	2.1	2.3	2.3	3.2	1.5	2.4	2.4	2.8
Dip30Shallow (Chi-Chi)	3.1	1.4	3.1	2.5	1.5	1.7	1.7	3.0
Dip30Deep	3.1	1.7	3.1	2.8	1.6	2.2	2.2	3.3

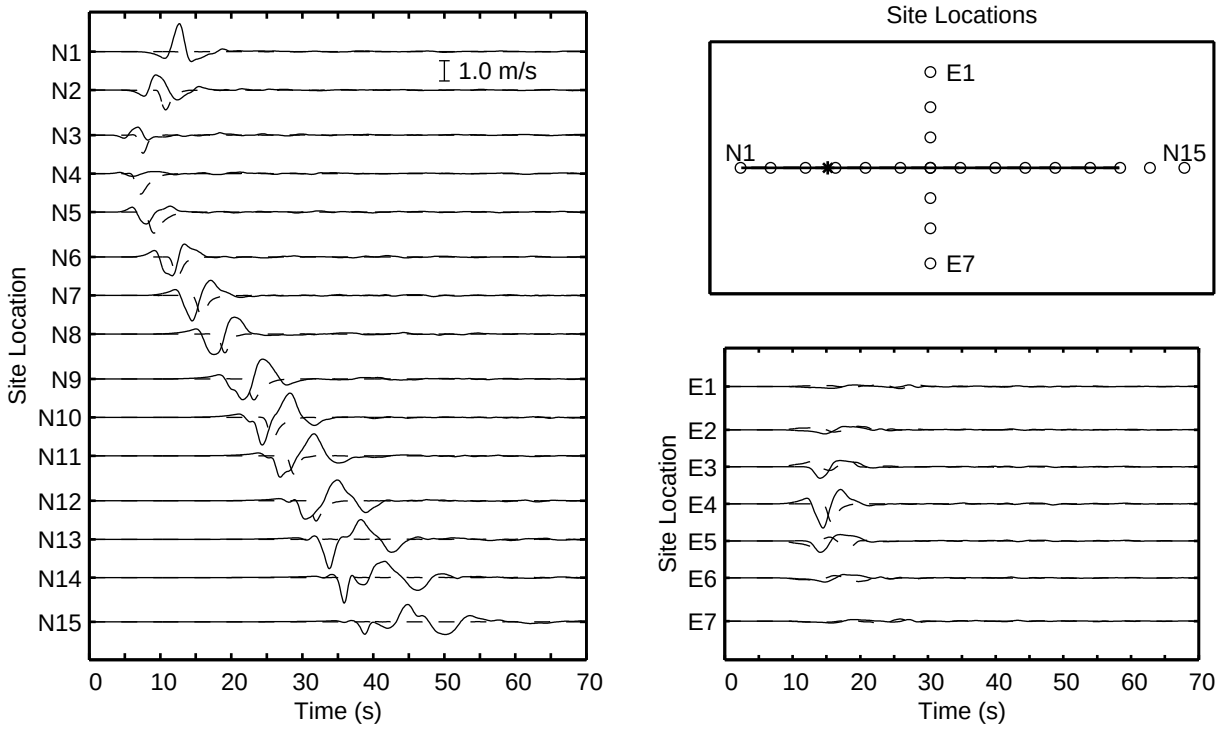

Figure 9. Velocity time histories along a north-south line over the trace of the fault (left) and along an east-west line passing over the center of the fault (lower right) for scenario Dip90Shallow. The two horizontal components are denoted by the solid line (east-west) and the dashed line (north-south). The diagram in the upper right identifies the locations of the sites (open circles) relative to the fault trace (solid line) and the epicenter (asterisk). On the north-south line the slip time histories dominate the north-south component, whereas the Love waves dominate the east-west component. The motions on the east-west line are small except near the fault trace.

Along the north-south line, the vertical components are largest along most of the fault trace, whereas off the north end of the fault the east-west components are largest. The sites along the east-west line indicate that, at the center of the fault, the strongest motion remains concentrated near the surface trace. However, from the maximum displacements and velocities (figure 7) we know that the region northwest of the northern portion of the fault also experiences strong shaking from the Love and Rayleigh waves.

Maintaining the hypocenter at the shallow location while further decreasing the dip of the fault and increasing the slip rake angle means the rupture propagates predominantly in the mode-III direction (perpendicular to the slip direction). In our limiting case of the 30 degree dipping fault with pure thrust motion, the velocity time histories displayed in figure 11 indicate that the slip time histories and Rayleigh waves control the motion; Love waves are much less prominent. At sites along the north-south line, the east-west components generally correspond to the slip time

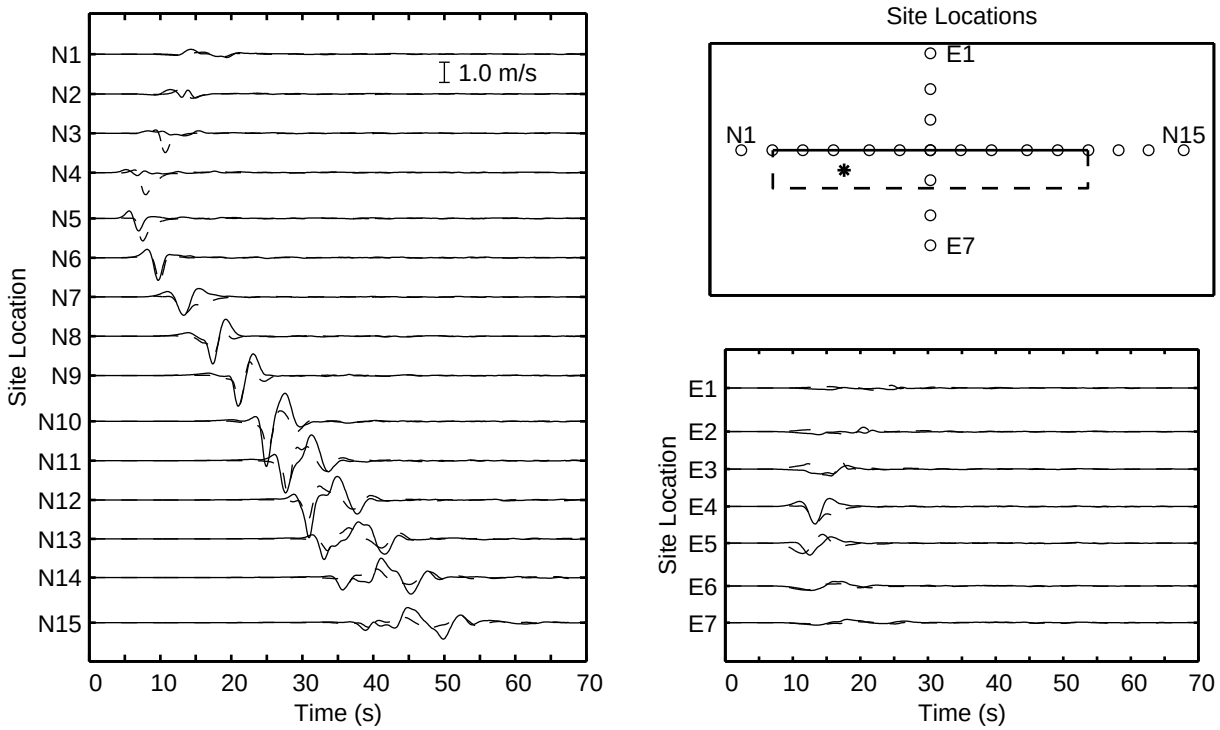

Figure 10. Velocity time histories along a north-south line over the trace of the fault (left) and along an east-west line passing over the center of the fault (right) for scenario Dip60Shallow. The two horizontal components are denoted by the solid line (east-west) and the dashed line (north-south). The diagram in the upper right identifies the locations of the sites (open circles) relative to the fault trace (solid line), the buried edges of the fault (dashed lines), and the epicenter (asterisk). The presence of large-amplitude Love and Rayleigh waves results in all three velocity components having similar amplitudes at sites along the north-south line.

history (the negative amplitude means the hanging wall motion is to the west), whereas the retrograde motions of the Rayleigh waves dominate the north-south and vertical components. On the east-west line, the shallow dip of the fault causes stronger motions on the hanging wall away from the fault trace compared with the motions from scenarios with the more steeply-dipping faults.

Shifting the hypocenter from the shallow location to the deep location (5 km up-dip from the bottom center of the fault) creates a more bilateral rupture. For the 60 degree dipping fault, we find the velocity waveforms retain the same general shape in scenario Dip60Deep as in scenario Dip60Shallow. In the northern half of the domain, the rupture propagates over a shorter distance in the direction of slip which, away from the fault, reduces both the amplitude of the ground motions and the duration of shaking.

For the case of pure thrust motion (with a fault dip angle of 30 degrees), the mode-II direction corresponds to up-dip rupture, so the location of the hypocenter near the bottom center of the fault increases the amount of mode-II rupture. Consequently, we observe larger amplitude motions in scenario Dip30Deep compared with scenario Dip30Shallow (Chi-Chi). This is especially true for the east-west line over the center of the fault. Additionally, although the vertical component for the site on the north-south line located directly up-dip from the hypocenter is about the same for the two scenarios, the vertical components at the surrounding locations dramatically increase for the deep hypocenter. Finally, with the deep hypocenter single-sided pulses characterize the velocity time histories along the fault trace, whereas off the ends of the fault the motion is characterized by double-sided pulses associated with the Rayleigh waves.

Response Spectra

Acceleration response spectra provide an additional tool for evaluating the severity of shaking associated with the earthquake ruptures. We compute the horizontal acceleration response spectra for five percent of critical damping after rotating the ground motions into the direction of the maximum peak-to-peak velocity at each location. We first focus on the response spectrum for a few select periods over the entire ground surface before examining spectra at a single site at a higher frequency resolution.

Figure 12 gives the response spectra on the entire ground surface for scenario Dip90Shallow at periods of 2.0, 3.0, 4.0, and 5.0 seconds. Several local maxima in the response spectra exceed 0.4 g; values greater than 0.6 g occur off the two ends of the fault for a period of 3.0 s. Although not immediately evident in the contour plots of the response spectra in figure 12, the spatial distributions become smoother at longer periods due to the larger wavelengths of the surface waves that control the response.

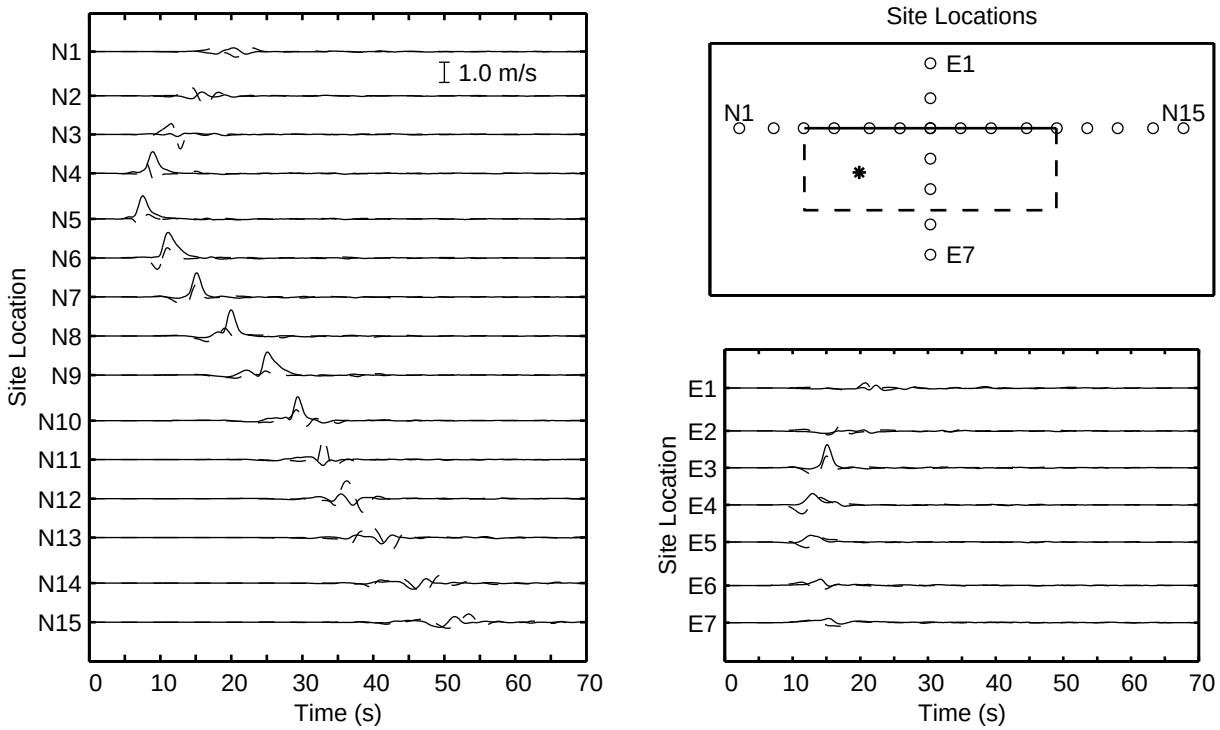

Figure 11. Velocity time histories along a north-south line over the trace of the fault (left) and along an east-west line passing over the center of the fault (right) for scenario Dip30Shallow (Chi-Chi). The two horizontal components are denoted by the solid line (east-west) and the dashed line (north-south). The diagram in the upper right identifies the locations of the sites (open circles) relative to the fault trace (solid line), the buried edges of the fault (dashed lines), and the epicenter (asterisk). Sites along the surface trace of the fault on the hanging wall show the slip time history on the east-west component, whereas the retrograde motion of the Rayleigh waves controls the north-south and vertical components. The ground motions are significantly larger on the hanging wall in this scenario compared with scenarios with the same hypocenter and steeper dipping faults.

The response spectra for scenario Dip60Shallow, shown in figure 13, display a complex spatial distribution northwest of the northern half of the fault. These complex variations arise from the presence of both Love and Rayleigh waves which have different radiation patterns; they create similar patterns in the distribution of the maximum peak-to-peak velocities (figure 7). The greater wavelengths associated with the longer period surface waves smooth these patterns as the period increases. As expected based on the larger ground motions for scenario Dip60Shallow compared with the strike-slip scenario Dip90Shallow, the response spectra for all four periods contain many local maxima exceeding 0.6 g with some greater than 0.8 g.

As we continue to decrease the dip angle of the fault and increase the slip rake angle, the response spectra values decrease in accordance with the smaller ground motions. For scenario Dip30Shallow (Chi-Chi)the response spectra in figure 14 contain only small regions with values greater than 0.4 g. We observe smoother variations for longer periods along with some minor fluctuations in the distribution with changes in period, but the largest values continue to coincide with the peaks in the Rayleigh-wave radiation pattern that extend off the northwest and southwest corners of the fault at angles of about 45 degrees.

For scenario Dip60Deep where the hypocenter sits 5.0 km up-dip from the bottom center of the 60 degree dipping fault, as opposed to mid-depth at the southern quarter point of the fault, the horizontal acceleration response spectra values decrease significantly from those observed for scenario Dip60Shallow with values exceeding 0.6 g over only small, limited areas. This stems from the lower amplitude ground motions. However, the spatial distribution retain a similar complex shape due to the combination of Love and Rayleigh waves that dominate the ground motions. With a hypocenter slightly up-dip from the bottom center of the fault and pure thrust motion in scenario Dip30Deep, the acceleration response spectra exhibit a significant change in shape compared with a mid-depth hypocenter at the southern quarter point of the fault. The values are greater over a larger region up-dip from the hypocenter and are much larger near the southwest corner of the fault (a region where the ground motions also increase). In contrast to scenario Dip30Shallow (Chi-Chi) where the spectral values rarely exceed 0.4 g, the spectral values exceed 0.4 g over a significant area for a period of 3.0 s and reach 0.6 g at some locations for a period of 2.0 s.

In order to illustrate the variation in the response spectra as a more continuous function of period, we examine the horizontal acceleration response spectra at site N10, which sits on the hanging wall of the fault trace 30 km north of the

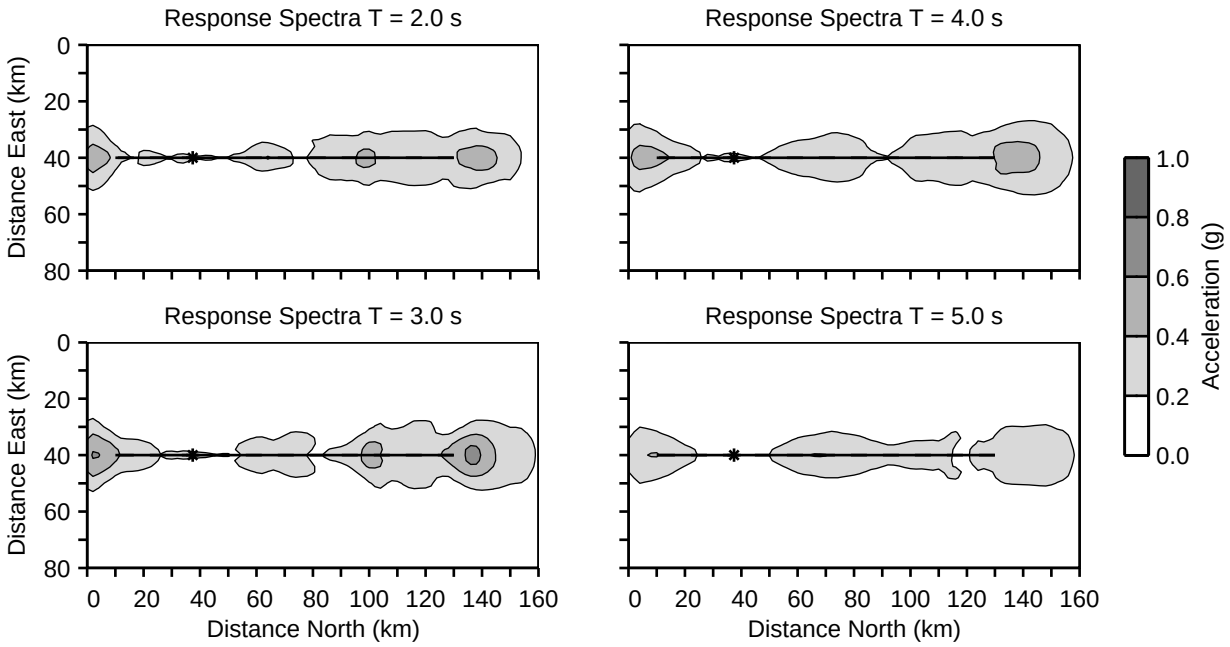

Figure 12. Horizontal acceleration response spectra on the ground surface for five percent of critical damping at four periods for scenario Dip90Shallow. The thick solid line shows the surface trace of the fault and the asterisk identifies the epicenter. The spectra are computed with ground motions resolved along the direction of the maximum peak-to-peak velocity.

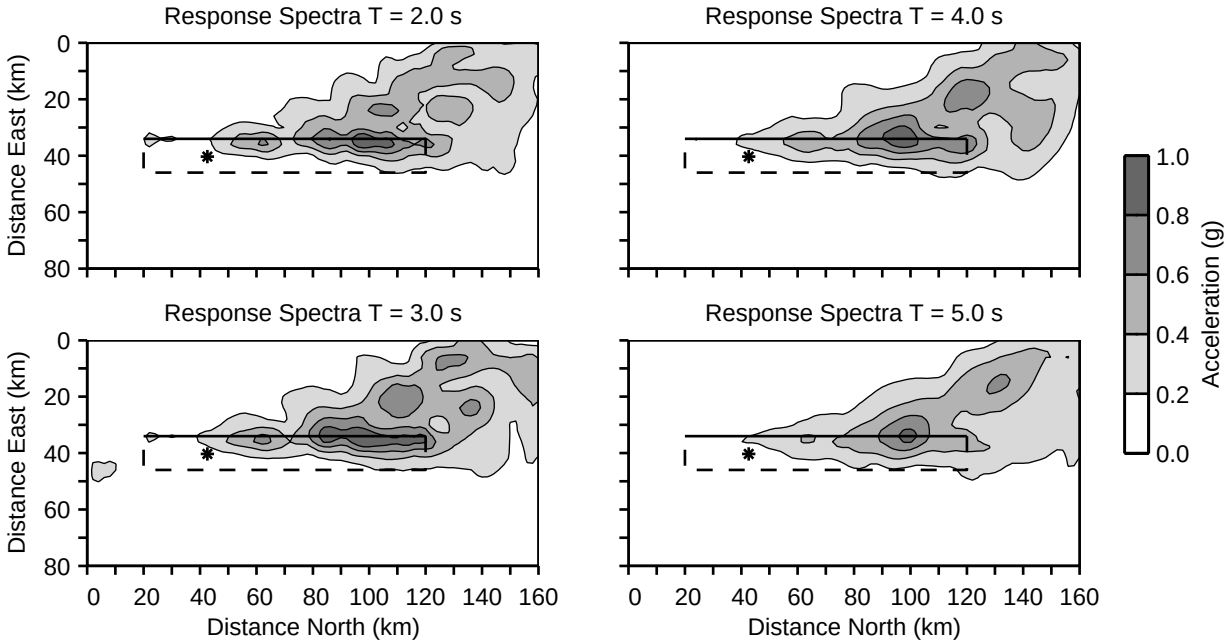

Figure 13. Horizontal acceleration response spectra on the ground surface for five percent of critical damping at four periods for scenario Dip60Shallow. The thick solid line shows the surface trace of the fault, the thick dashed line indicates the surface projection of the buried edges of the fault, and the asterisk identifies the epicenter. The spectra are computed with ground motions resolved along the direction of the maximum peak-to-peak velocity. The response spectra reflect both the large-amplitude ground motions and the complex spatial distribution of shaking created by the presence of Love and Rayleigh waves.

center of the fault. This site experiences the effects of rupture directivity in all ten scenarios and generally undergoes some of the strongest motion. Figure 15 shows the response spectra at this site for periods from 2.0 to 12 seconds. The spectra reaffirm that the ground motion in scenario Dip60Shallow is the most severe with values between 0.9 g and 1.0 g over a period range of 2.0 to 5.0 seconds. Likewise, the motion in scenario Dip30Shallow (Chi-Chi) is the most benign over nearly the entire range of periods. At site N10 the response spectra for all scenarios fall below 0.4 g for periods above about 9 seconds.

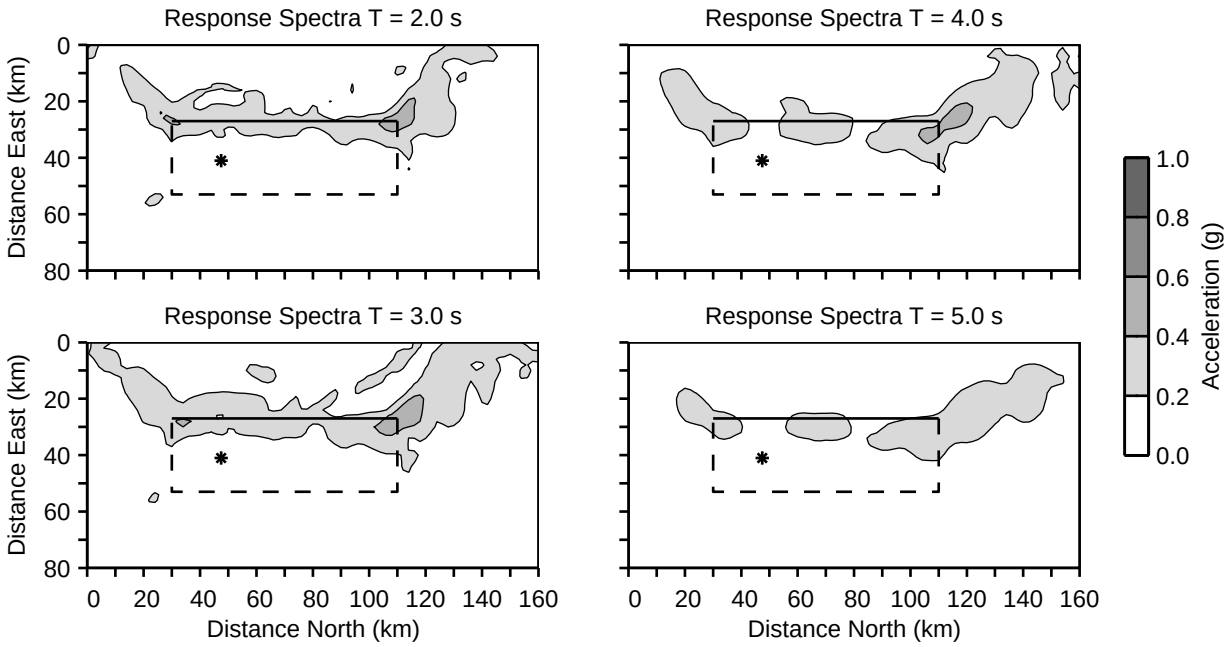

Figure 14. Horizontal acceleration response spectra on the ground surface for five percent of critical damping at four periods for scenario Dip30Shallow (Chi-Chi). The thick solid line shows the surface trace of the fault, the thick dashed line indicates the surface projection of the buried edges of the fault, and the asterisk identifies the epicenter. The spectra are computed with ground motions resolved along the direction of the maximum peak-to-peak velocity. The maxima in the response spectra occur at peaks in the Rayleigh-wave radiation pattern which extend in the southwest and northwest directions from the top corners of the fault.

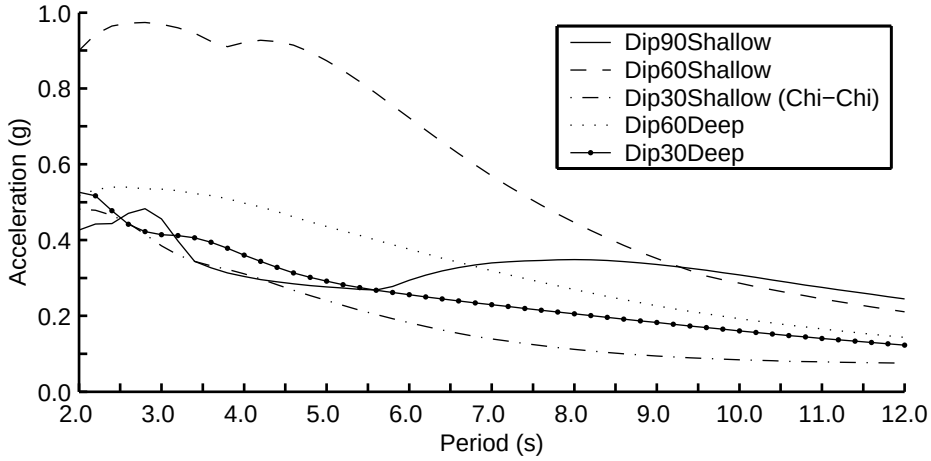

Figure 15. Horizontal acceleration response spectra at site N10 for scenarios Dip90Shallow, Dip60Shallow, Dip30Shallow (Chi-Chi), Dip60Deep, and Dip30Deep. Site N10 sits on the hanging wall of the fault trace 30 km north of the center of the fault. The spectra are computed with ground motions resolved along the direction of the maximum peak-to-peak velocity. The values above 0.9 g at the shorter periods in the response spectrum for scenario Dip60Shallow correspond to the strong level of shaking associated with the large-amplitude Love and Rayleigh waves.

Discussion

We observe large-amplitude long-period ground motions in all ten scenarios. The choices for the values of final slip, peak slip rate (slip duration), and rupture speed all affect the amplitude of the ground motion (Aagaard *et al.*, 2001). As discussed in the section on the choice of earthquake parameters, the values selected for these simulations fall within reasonable ranges, so the level of shaking should be indicative of the long-period motions in real earthquakes. Furthermore, the trends with respect to the style of the faulting depend only on the relative values of these parameters, and these values are essentially the same in all ten scenarios.

In order to gauge how the severity of shaking changes on a large scale as we transition from pure strike-slip faulting on a vertical fault to thrust faulting on a 30 degree dipping fault, we consider three aggregate measures of ground motion: the area on the ground surface where a given level of displacement or velocity is exceeded, how fast the displacements and

velocities on the ground surface decay with distance from the fault, and the radiated energy.

Area Subjected to Levels of Ground Motion

Figure 16 gives the areas on the ground surface where the maximum displacements or maximum peak-to-peak velocities exceed a given value for each of the five scenarios with the shallow hypocenter (mid-depth at the southern quarter point of the fault), where each scenario corresponds to a different dip angle of the fault. In all five cases very large areas (more than $1000\,\mathrm{km}^2$) receive long-period ground motions with displacements or peak-to-peak velocities greater than $1.3\,\mathrm{m}$ or $1.0\,\mathrm{m/s}$. In accordance with the observations noted earlier, the amount of rupture directivity toward the surface controls the amplitude of the motion, so that the largest areas subjected to strong shaking occur in the scenarios with a fault dip angle of 60 or 75 degrees. Moreover, at the strongest levels of shaking, these areas far exceed the corresponding areas for the other scenarios.

The case of pure strike-slip motion on a vertical fault generally falls in the middle ground below the 60 and 75 degree dipping fault scenarios and above the 45 and 30 degree dipping fault scenarios. The curves relating area and maximum displacements for scenarios Dip30Shallow and Dip45Shallow closely follow one another, but the curve relating area and maximum peak-to-peak velocities for scenario Dip45Shallow lies well to the right of the one for scenario Dip30Shallow (Chi-Chi). Thus, for the shallow hypocenter the case of pure thrust motion on a 30 degree dipping fault results in the smallest area subjected to a given level of peak-to-peak velocity.

Compared with the scenarios with the shallow hypocenter, those with the deep hypocenter ($5.0\,\mathrm{km}$ up-dip from the bottom center of the fault) exhibit much less variation in the area experiencing a given level of shaking for the various combinations of fault dip and slip rake angles as illustrated in figure 17. The more central hypocenter near the bottom of the fault leads to less variation in the distance the rupture propagates in the mode-II direction (direction parallel to slip), because the amount of along-strike rupture decreases while the amount of up-dip rupture increases. This reduces the amount of mode-II rupture in the cases with small slip rake angles, which were dominated by mode-II rupture for the shallow hypocenter, and increases the amount of mode-II rupture in the cases with large slip rake angles, which were dominated by mode-III rupture for the shallow hypocenter. The 60 degree dipping fault with a slip rake angle of 45 degrees generally continues to produce the largest areas subjected to a given level of shaking with this different hypocenter, but the curve for pure thrust motion on the 30 degree dipping fault shifts toward the middle ground. For some ranges of moderate peak-to-peak velocities, the case of pure thrust motion on the 30 degree dipping fault has the largest areas where these levels of motion are exceeded.

Figure 18 illustrates how changing the hypocenter for pure thrust motion on the 30 degree dipping fault alters the curves relating the area experiencing a given level of displacement and peak-to-peak velocity. Changing the hypocenter has only a small effect on the curve for the maximum displacements, because the slip distribution, which remains the same, largely controls the amplitude of the displacements. On the other hand, moving the hypocenter from the shallow location to the deep location shifts the curve for the peak-to-peak velocities toward larger velocities as a result of the increase in the amount of mode-II (in this case up-dip) rupture.

Decay in Ground Motion with Distance

We want to characterize how the ground motions decay with distance from the fault, while including the effects of rupture directivity and the unpredictability of the hypocenter. We consider identical events occurring along an infinite fault and superimpose the distributions of the maximum displacements and velocities for a given scenario such that the faults lie end to end as illustrated in figure 19. At each location we select the largest values across all of the overlapping domains, and then average along the strike of the fault to obtain the average motion on each side of the fault at a given distance. We compare the decay in the level of motion with that of the near-source factor, N_v, from the 1997 Uniform Building Code (ICBO, 1997). Figure 20 displays the UBC near-source factor for each of the five fault geometries. On the up-dip (west) side of the fault, the near-source factors are identical, but on the down-dip (east) side of the fault, the near-source factors for shallower dip angles remain high before decreasing at greater distances from the fault.

The variation in the ground motions along the strike of the fault creates a complex decay in the ground motions with distance from the fault as demonstrated for scenario Dip60Shallow in figure 21. The 60 degree dip angle of the fault produces an asymmetric distribution of the maximum displacements and maximum peak-to-peak velocities with a much slower decay with distance on the up-dip (west) side compared with the down-dip (east) side. The sites with the largest values fall within the region of the highest near-source factor, but the peak of the mean falls near the up-dip boundary.

Figures 22 through 24 show the decay of the maximum displacements and maximum peak-to-peak velocities with distance from the fault for each of the two hypocenters for the scenarios with fault dip angles of 90, 60, and 30 degrees. We find that moving the hypocenter causes no significant change in the shape of the mean distribution, e.g., location of the peak. However, the deep hypocenter yields smaller mean values for fault dip angles of 90 and 60 degrees due to the bilateral nature of the rupture. On the other hand, this hypocenter gives larger mean values for a fault dip angle of 30 degrees, because the amount of up-dip rupture increases. The asymmetry with respect to the locations that bound the smallest and largest UBC near-source values grows as the

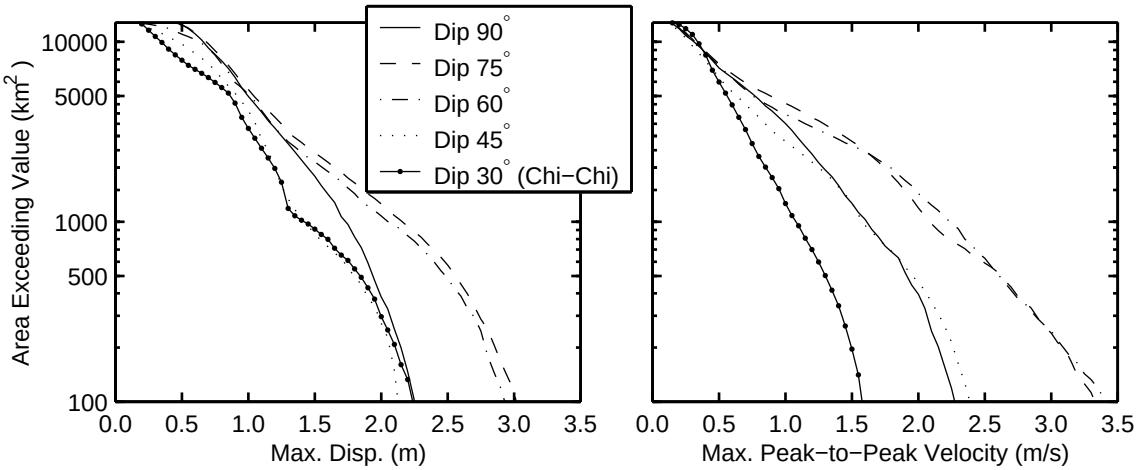

Figure 16. Area on the ground surface where the maximum horizontal displacements (left) and maximum peak-to-peak horizontal velocities (right) exceed a given value for scenarios with the shallow hypocenter. In all five scenarios areas greater than $1000\,\mathrm{km}^2$ undergo displacements exceeding $1.3\,\mathrm{m}$ and peak-to-peak velocities exceeding $1.0\,\mathrm{m/s}$ with much larger areas for scenarios Dip60Shallow and Dip75Shallow.

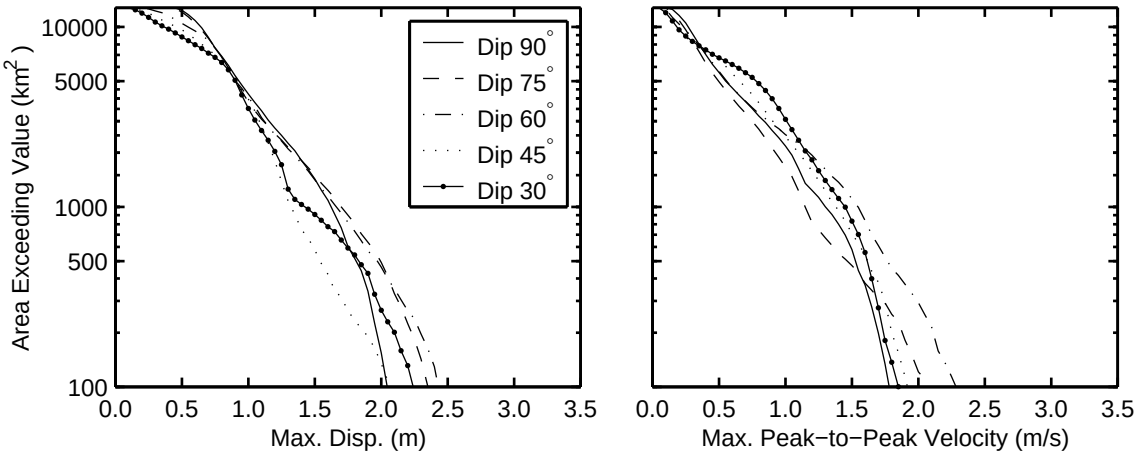

Figure 17. Area on the ground surface where the maximum horizontal displacements (left) and maximum peak-to-peak horizontal velocities (right) exceed a given value for scenarios with the deep hypocenter. Shifting the hypocenter to near the bottom center of the fault leads to much smaller variations in the area subjected to a given level of shaking across the five fault dip and slip rake angle pairs.

dip becomes shallower with much larger peak-to-peak velocities on the up-dip (west) side compared with the down-dip (east) side.

In figure 25 we compare the mean maximum displacements and mean maximum peak-to-peak velocities for scenarios with the shallow hypocenter across the five fault dip angles. On the down-dip (east) side of the fault at distances between 10 and 30 kilometers, the mean values vary remarkably little with the dip angle of the fault. At closer distances and on the up-dip (west) side of the fault, the mean maximum values span a larger range of values; they are lowest for pure thrust motion on the 30 degree dipping fault and up to two times greater for oblique slip on the 60 and 75 degree dipping faults. These differences arise from the large amount of rupture directivity that occurs for the combination of the shallow hypocenter with the steeply dipping fault geometries and the small amount of rupture directivity that occurs for the same hypocenter with the shallow dipping fault geometries.

As we found with the area where the maximum motion exceeds a given level, we find less variation in how the mean maximum motion decays with distance from the fault for the deep hypocenter (figure 26) than for the shallow hypocenter (figure 25). Near the trace of the fault, the mean displacements and mean peak-to-peak velocities exhibit only small variations. Likewise, the mean peak-to-peak velocities on the down-dip (east) side of the fault decay in nearly an identical fashion for all five fault dip angles. However, on the up-dip (east) side of the fault, the mean displacements and mean peak-to-peak velocities decay at varying rates for the different fault dip angles. The values decay rapidly for the steeply dipping faults and significantly more slowly for the shallow dipping faults, although the displacements for the 30 degree dipping fault drop dramatically from the hanging wall (east side) to the footwall (west side) before decaying slowly with distance.

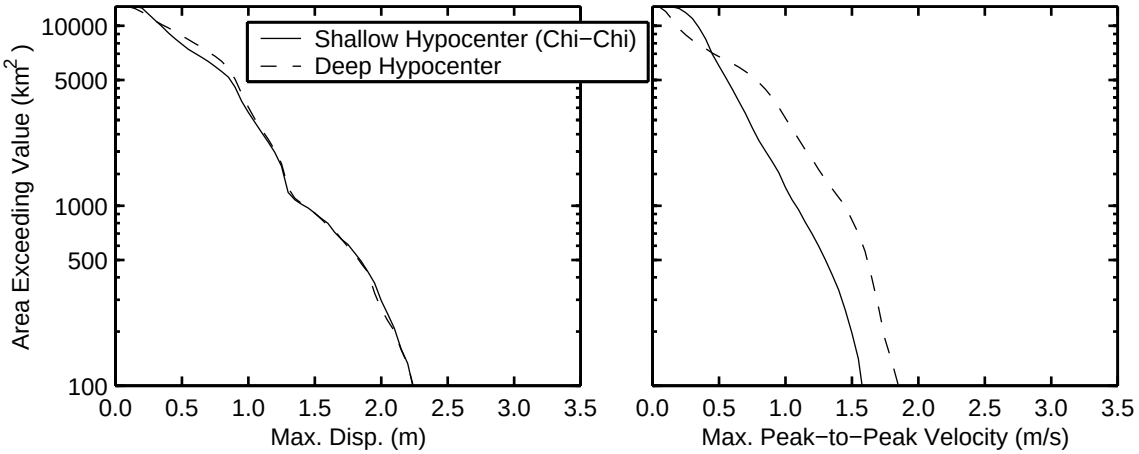

Figure 18. Area on the ground surface where the maximum horizontal displacements (left) and maximum peak-to-peak horizontal velocities (right) exceed a given value for scenarios Dip30Shallow (Chi-Chi) and Dip30Deep. For the 30 degree dipping fault, the hypocenter has a strong effect on the area subjected to a given level of peak-to-peak velocity, but has little effect on the area subjected to a given level of displacement.

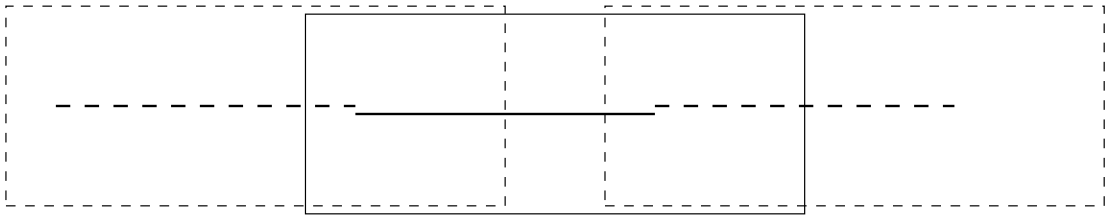

Figure 19. Illustration of how an infinite fault is created from the finite fault in order to examine the decay in ground motion amplitudes with distance from the fault.

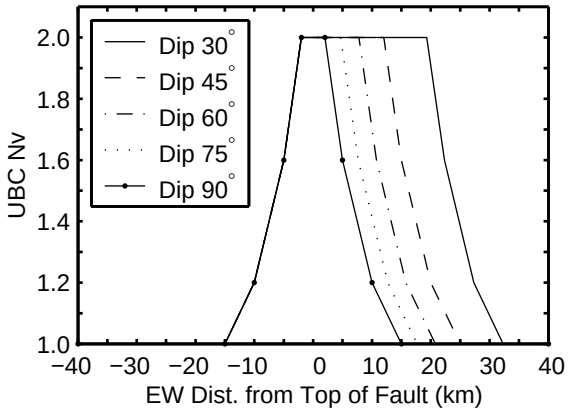

Figure 20. UBC near-source factor N_v for a type A source for each fault geometry. The dip angle of the fault affects only the location where the decay begins on the hanging wall (east) side of the fault.

Radiated Energy

The radiated energy (figure 27) displays the same general trends across the ten scenarios as the velocity amplitudes on the ground surface. The radiated energy corresponds to the energy in the seismic waves in the simulation. Consequently, they do not account for energy at periods shorter than 2.0 s. The two scenarios with the largest amplitude ground motions (scenarios Dip60Shallow and Dip75Shallow) also radiate the largest amount of energy (1.1×10^{16} J). Scenario Dip90Shallow radiates slightly less energy (9.8×10^{15} J). As expected from the amplitude of the ground motions, the smallest radiated energy of 5.5×10^{15} J occurs in scenario Dip30Shallow (Chi-Chi). Moving the hypocenter to the deep location results in a 23% increase in the amount of radiated energy for the 30 degree dipping fault, while it decreases the radiated energy for the other fault geometries. Scenarios Dip75Deep, Dip60Deep, and Dip45Deep all radiate about 7.2×10^{15}J. Consequently, in accordance with the level of long-period shaking, the scenarios with the deep hypocenter exhibit much less variation in the radiated energy than those with the shallow hypocenter. Overall, we find that the variations in the radiated energy closely follow the trends in the relative velocity amplitudes on the ground surface.

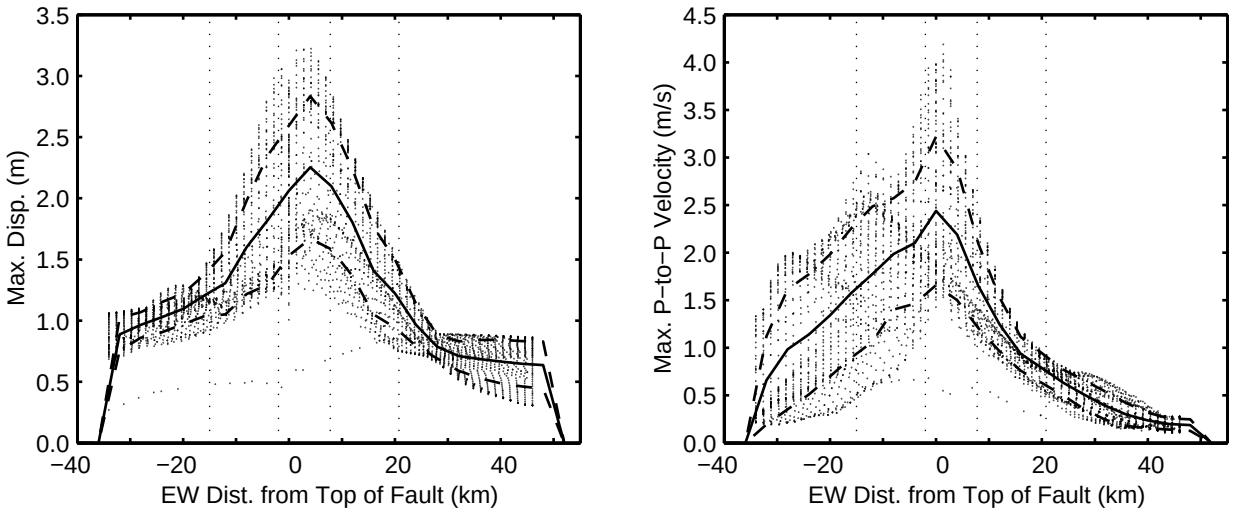

Figure 21. Maximum horizontal displacements and maximum peak-to-peak horizontal velocities as a function of distance from the fault for scenario Dip60Shallow. The dots indicate the values at locations on the ground surface, the solid line delineates the mean, and the dashed lines correspond to one standard deviation above and below the mean. The vertical dotted lines bound the locations where the UBC near-source factor N_v is equal to 2 (inner pair) and equal to 1 (outer pair). The fault dip angle of 60 degrees cause the asymmetry in the distributions of the values, whereas local extrema in the distributions result in a complex decay with distance from the fault.

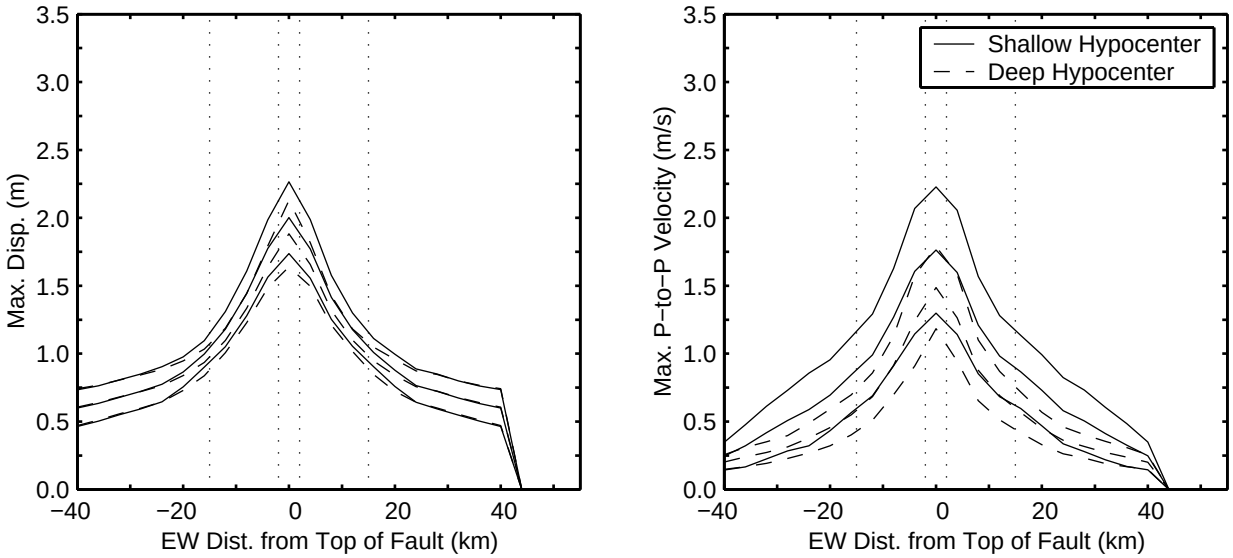

Figure 22. Maximum horizontal displacements and maximum peak-to-peak horizontal velocities as a function of distance from the fault for scenarios Dip90Shallow and Dip90Deep. Scenario Dip90Deep has a deep hypocenter that is centrally located along the strike of the fault which results in a bilateral rupture. The three lines (solid or dashed) for each hypocenter correspond to the mean and the mean plus or minus one standard deviation. The vertical dotted lines bound the locations where the UBC near-source factor N_v is equal to 2 (inner pair) and equal to 1 (outer pair). The maximum displacements and maximum peak-to-peak velocities decay rapidly with distance from the fault.

Implications for Analysis of 1999 Chi-Chi Earthquake

Scenario Dip30Shallow with pure thrust motion on a 30 degree dipping fault with the shallow hypocenter approximately matches the geometry of 1999 Chi-Chi earthquake in Taiwan (Huang *et al.*, 2000; Ma *et al.*, 2000; Johnson *et al.*, 2001; Ma *et al.*, 2001; Ji *et al.*, 2001). Our choice of a fault area of 2400 km^2 and an average slip of 2.9 m results in a moment magnitude of 7.4 compared with estimates of 7.6–7.7 for the Chi-Chi earthquake. Nevertheless, scenario Dip30Shallow provides a good general representation of the earthquake.

For the shallow hypocenter scenario Dip30Shallow generates the smallest amplitude ground motions of all five fault geometries. Near the surface trace of the fault and in the region up-dip from the fault, the mean maximum horizontal peak-to-peak velocities for the other four scenarios far exceed those of scenario Dip30Shallow. For example, the greatest mean maximum peak-to-peak velocities for the other four scenarios range from 1.8 m/s to 2.6 m/s compared

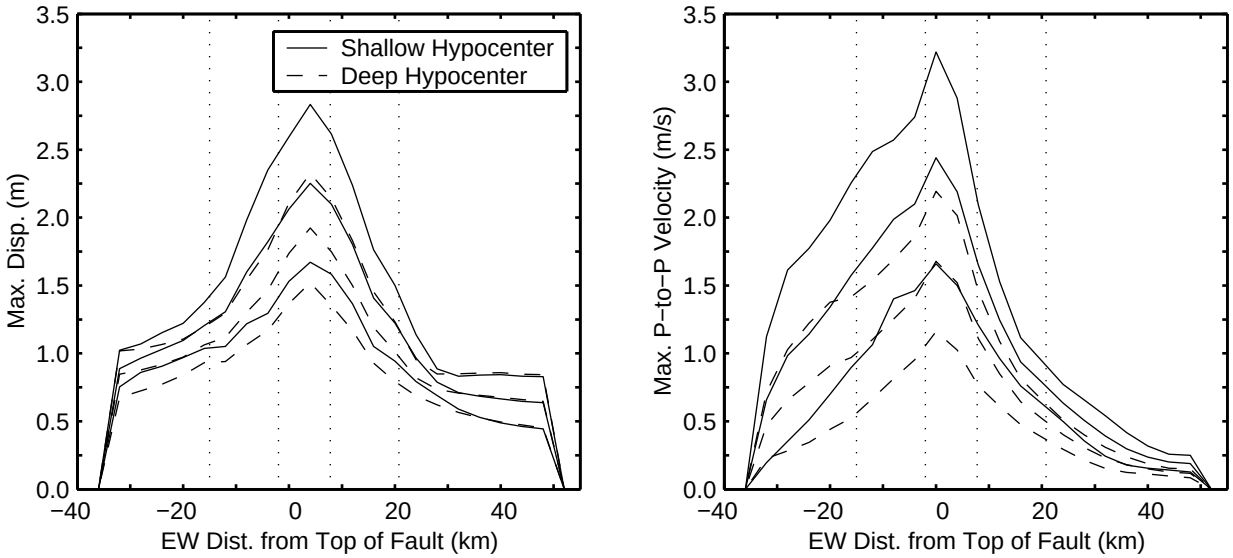

Figure 23. Maximum horizontal displacements and maximum peak-to-peak horizontal velocities as a function of distance from the fault for scenarios Dip60Shallow and Dip60Deep. The three lines (solid or dashed) for each hypocenter correspond to the mean and the mean plus or minus one standard deviation. The vertical dotted lines bound the locations where the UBC near-source factor N_v is equal to 2 (inner pair) and equal to 1 (outer pair). The directivity of the rupture produces an asymmetric distribution of the values with a much slower decay with distance and greater variation about the mean on the up-dip (west) side of the fault.

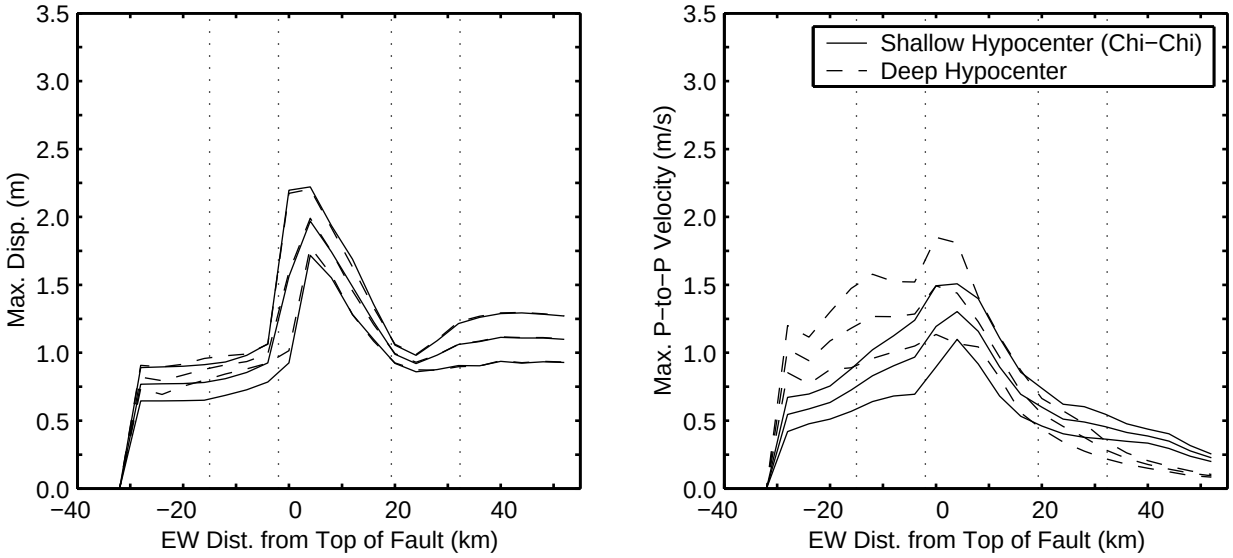

Figure 24. Maximum horizontal displacements and maximum peak-to-peak horizontal velocities as a function of distance from the fault for scenarios Dip30Shallow (Chi-Chi) and Dip30Deep. The three lines (solid or dashed) for each hypocenter correspond to the mean and the mean plus or minus one standard deviation. The vertical dotted lines bound the locations where the UBC near-source factor N_v is equal to 2 (inner pair) and equal to 1 (outer pair). Shifting the hypocenter toward the bottom of the fault results in more up-dip rupture and increases the peak-to-peak velocities near the fault and at greater distances from the fault on the up-dip (west) side.

with $1.3\,\mathrm{m/s}$ for scenario Dip30Shallow. Even in the case of the mean maximum displacements on the hanging wall near the fault trace, where there is relatively little variation, the values for Dip30Shallow fall at the low end of the spectrum. The largest ground motions occur for a small rake angle and a steeply dipping fault; these geometries create a significant amount of rupture directivity and generate both Love and Rayleigh waves with large amplitudes. As a result, in scenario Dip60Shallow the horizontal acceleration response spectrum at site N10 approaches $1\,\mathrm{g}$ over a broad range of periods (figure 15).

Additionally, a deeper hypocenter than the shallow location for thrust motion on the 30 degree dipping fault yields more rupture directivity and leads to larger ground motions. Scenario Dip30Deep illustrates this for a hypocenter located

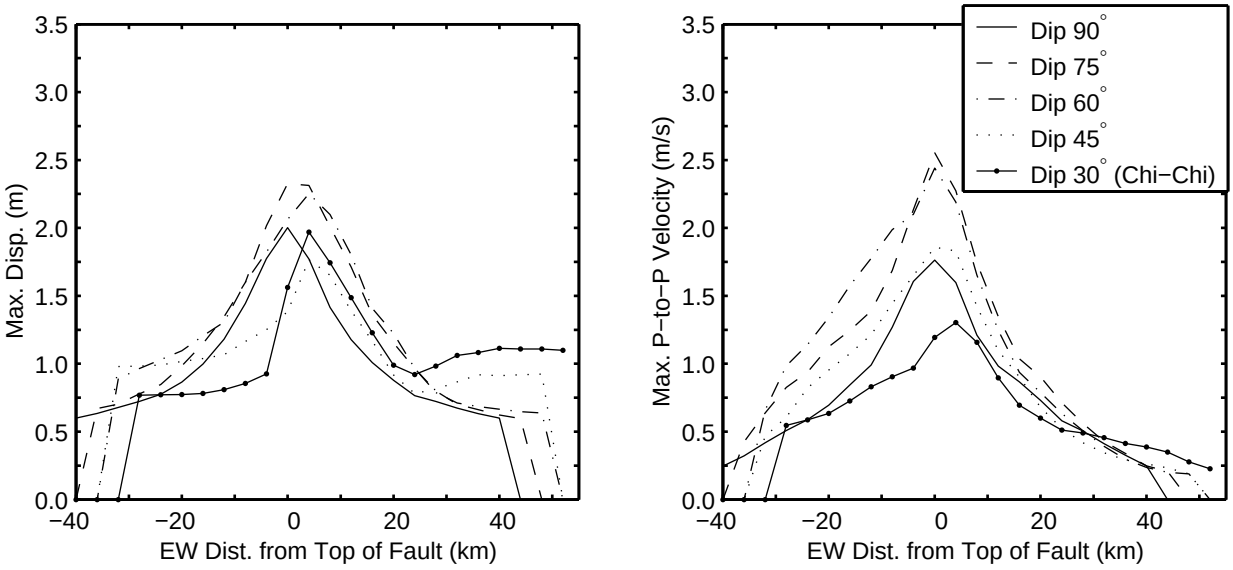

Figure 25. Mean maximum horizontal displacements and mean maximum peak-to-peak horizontal velocities as a function of distance from the fault for scenarios with the shallow hypocenter. Although the mean values do not dramatically differ on the down-dip (east) side of the fault, they span a wide range of values both up-dip (west) of the fault and near the fault trace.

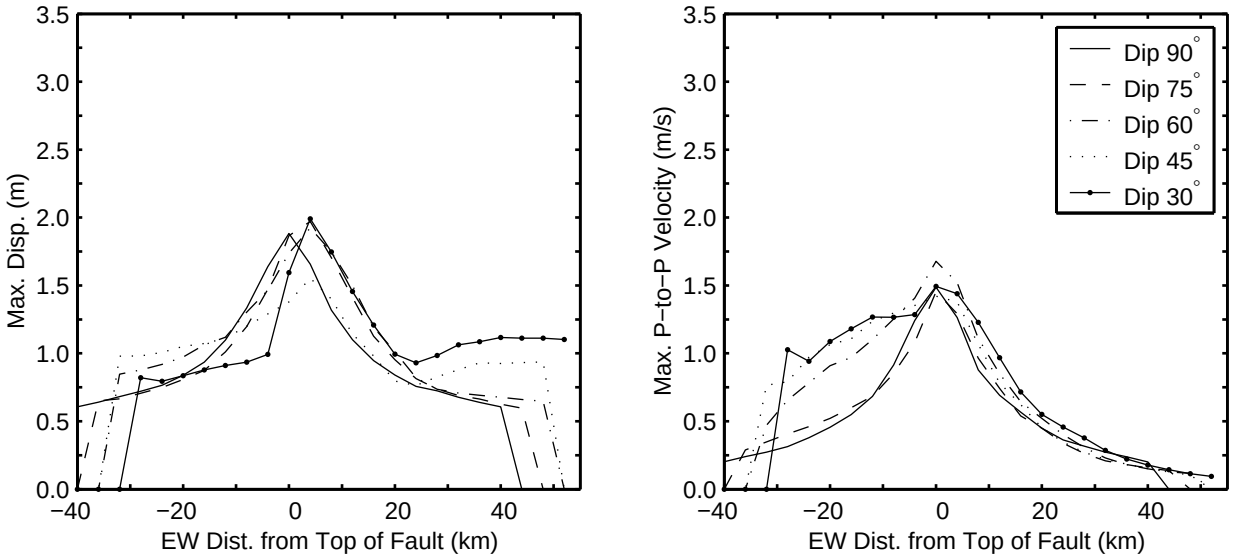

Figure 26. Mean maximum horizontal displacements and mean maximum horizontal peak-to-peak velocities as a function of distance from the fault for scenarios with the deep hypocenter. The mean maximum values generally fall within a smaller range for the deep hypocenter compared with the shallow hypocenter. On the up-dip (west) side of the fault, the mean velocities decay more slowly as the fault dip becomes shallower.

near the bottom center of the fault. Although the greatest mean maximum horizontal displacement is still 2.0 m, the greatest mean maximum peak-to-peak horizontal velocity increases from 1.3 m/s to 1.5 m/s. Furthermore, the area on the ground surface subjected to a given level of peak-to-peak velocity increases significantly for peak-to-peak velocities greater than 0.5 m/s (figure 18).

Of all ten scenarios considered in this study, which range from pure strike-slip motion on a vertical fault to pure thrust motion on a shallow dipping fault, the one most like the Chi-Chi earthquake produces the mildest long-period ground motion. Up-dip from the fault the ground motions for the other scenarios are significantly more severe, particularly for the case of predominantly strike-slip motion on steeply dipping faults. The increased level of long-period motion is evident in numerous measures of the ground shaking, including the response spectra, the area where the displacements and peak-to-peak velocities exceed a given level, and the mean maximum displacements and mean maximum peak-to-peak velocities at a given distance from the fault. These simulations appear to be consistent with large-amplitude motions being recorded only very close to the fault trace in the Chi-Chi earthquake (Huang *et al.*, 2000). The lack of rupture directivity caused the near-source ground motions to be dominated by the near-field (pseudo-static) motions.

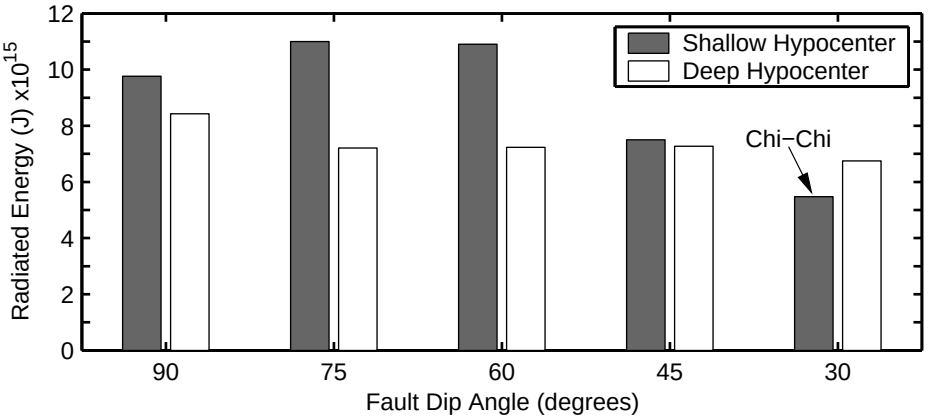

Figure 27. Radiated energy for each of the two hypocenters for each of the five different fault geometries. For predominantly along-strike, unilateral ruptures (shallow hypocenter) the steeply dipping faults radiate considerably more energy than the shallow dipping faults. For predominantly up-dip, bilateral ruptures (deep hypocenter) the radiated energies from the five scenarios exhibit much less variation.

Consequently, the ground motions decayed rapidly with distance from the fault trace. Had the hypocenter been much deeper or more centrally located along the strike of the rupture, we expect that the ground motions would have decayed less rapidly and been large over a much greater area.

Conclusions

Owing to the presence of shallow slip in the magnitude 7.4 earthquake simulations considered here, Love and/or Rayleigh waves dominate the ground motions with strike-slip faulting that tends to generate Love waves and thrust faulting that tends to generate Rayleigh waves. The amount of rupture toward the surface in the direction parallel to slip (mode-II direction and a local maximum in the shear-wave radiation pattern) controls the severity of the long-period shaking. For strike-slip faulting the shaking is most severe for unilateral rupture, while for thrust faulting the shaking is most severe for up-dip rupture from a deep hypocenter. Figure 28 summarizes how the direction of propagation and the slip rake angle affect the location and degree of rupture directivity. The directivity effect is maximized in the regions where the rupture propagates parallel to the slip vector.

When the hypocenter sits mid-depth at a fault quarter point, the largest ground motions occur for the 60 degree dipping fault, which has a slip rake angle of 45 degrees. This style of faulting generates large-amplitude Love and Rayleigh waves that lead to a maximum peak-to-peak horizontal displacement of 3.6 m and a maximum peak-to-peak velocity of 4.2 m/s. The mildest shaking (a maximum peak-to-peak velocity of 1.7 m/s) occurs for pure thrust motion on a 30 degree dipping fault because the rupture propagates primarily in the mode-III direction (in plane direction perpendicular to slip and a node in the shear-wave radiation pattern). This case closely matches the 1999 Chi-Chi earthquake and implies that a different style of faulting with a similar hypocenter would have led to large-amplitude ground motions over a broader area.

Shifting the hypocenter toward the bottom center of the fault results in less variation in the level of shaking across the five pairs of fault dip and slip rake angles considered. The bilateral nature of the ruptures reduces the ground motions for scenarios with predominantly strike-slip faulting, while the larger amount of up-dip rupture increases the ground motions for scenarios with predominantly thrust faulting. Thus, shifting the hypocenter of the Chi-Chi earthquake to a deep location, centrally located along the strike of the fault would significantly increase the amplitude of the ground motions due to the increase in distance the rupture propagates toward the surface parallel to the slip vector.

This set of simulations suggest that while the ground motions in the 1999 Chi-Chi earthquake in Taiwan may have been large at some locations, they occurred over a relatively small area because of the shallow hypocenter and predominantly unilateral rupture on the shallow-dipping fault with mostly thrust motion. The rupture propagated along a node in the shear-wave radiation pattern which limited the amount of rupture directivity. Consequently, we expect severe long-period ground motions over a much larger area when events of the same size occur with other styles of faulting or deeper hypocenters.

Acknowledgments

Access to the Hewlett-Packard V-Class computer, located at the California Institute of Technology, was provided by the Center for Advanced Computing Research.

This work was supported in part by the Pacific Earthquake Engineering Research Center through the Earthquake Engineering Research Centers Program of the National Science Foundation under award number EEC-9701568.

References

Aagaard, B. T. (1999). Finite-element simulations of earthquakes. Technical Report 99-03, California Institute of Technology, Earthquake Engineering Research Laboratory, Pasadena, CA.

Aagaard, B. T., J. F. Hall, and T. H. Heaton (2001, May). Characterization of near-source ground motions with earthquake simulations. *Earthquake Spectra 17*(2), 177–207.

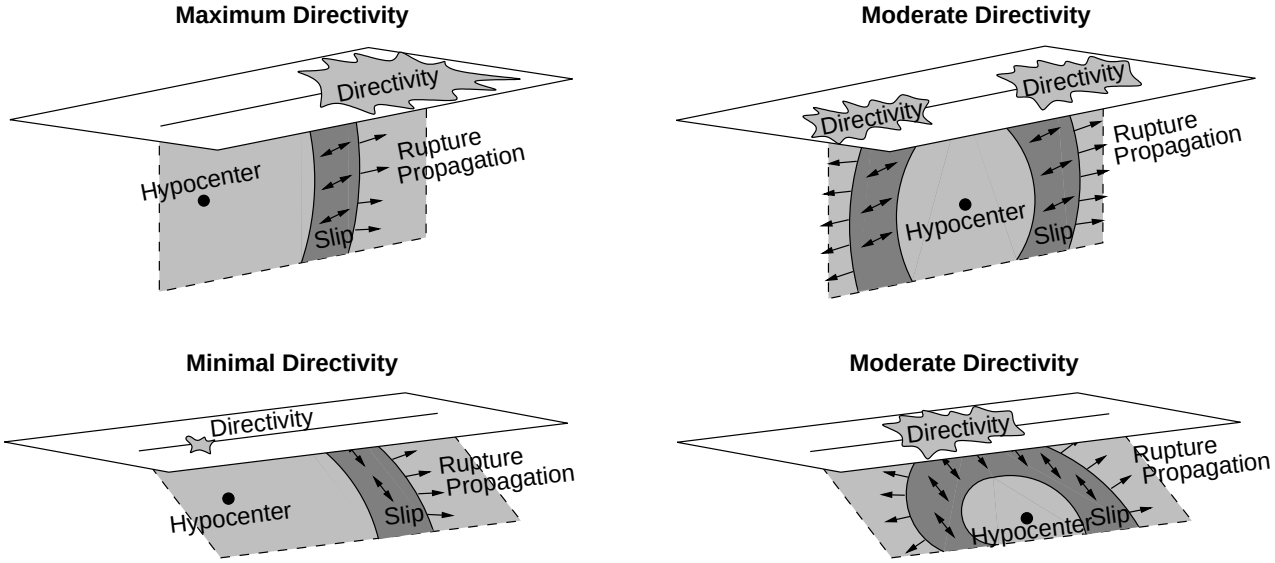

Figure 28. Summary of how the fault geometry and the slip rake angle affect the amount and location of rupture directivity as indicated by the size and location of the splotch on the ground surface. The top row illustrates two cases for a vertical fault with oblique motion, and the bottom row illustrates two cases for a shallow-dipping fault with thrust motion. The left column corresponds to predominantly along strike rupture (i.e., the shallow hypocenter), whereas the right column corresponds to predominantly bilateral or up-dip rupture (i.e., the deep hypocenter).

Aagaard, B. T., J. F. Hall, and T. H. Heaton (2002, December). Effects of fault dip and slip rake on near-source ground motions: Why the 1999 *M* 7.6 Chi-Chi, Taiwan, earthquake was relatively mild. Technical Report 2002/12, Pacific Earthquake Engineering Research Center, University of California, Berkeley, CA.

Aagaard, B. T., T. H. Heaton, and J. F. Hall (2001, December). Dynamic earthquake ruptures in the presence of lithostatic normal stresses: Implications for friction models and heat production. *Bulletin of the Seismological Society of America 91*(6), 1765–1796.

Allen, C. R., J. R. Brune, L. S. Cluff, and A. G. Barrows (1998, November/December). Evidence for unusually strong near-field ground motion on the hanging wall of the San Fernando fault during the 1971 earthquake. *Seismological Research Letters 69*(6), 524–531.

Andrews, D. (1976, November 10). Rupture velocity of plane strain shear cracks. *Journal of Geophysical Research 81*(32), 5679–5687.

Archuleta, R. J. and G. A. Frazier (1978, June). Three-dimensional numerical simulations of dynamic faulting in a half-space. *Bulletin of the Seismological Society of America 68*(3), 541–572.

Archuleta, R. J. and S. H. Hartzell (1981, August). Effects of fault finiteness on near-source ground motion. *Bulletin of the Seismological Society of America 71*(4), 939–957.

Boatwright, J., K. Thywissen, and L. Seekins (2001). Correlation of ground motion and intensity for the 17 January 1994 Northridge, California, earthquake. *Bulletin of the Seismological Society of America 91*(4), 739–752.

Day, S. M. (1982, December). Three-dimensional simulation of spontaneous rupture: The effect of nonuniform prestress. *Bulletin of the Seismological Society of America 72*(6), 1881–1902.

Graves, R. W. (1998, August). Three-dimensional finite-difference modeling of the San Andreas fault: Source parameterization and ground-motion levels. *Bulletin of the Seismological Society of America 88*(4), 881–897.

Hall, J. F., T. H. Heaton, M. W. Halling, and D. J. Wald (1995, November). Near-source ground motion and its effects on flexible buildings. *Earthquake Spectra 11*(4), 569–605.

Haskell, N. (1969, April). Elastic displacements in the near-field of a propagating fault. *Bulletin of the Seismological Society of America 59*(2), 865–908.

Heaton, T. H. (1990, November). Evidence for and implications of self-healing pulses of slip in earthquake rupture. *Physics of the Earth and Planetary Interiors 64*(1), 1–20.

Heaton, T. H. (1995). Overview of seismological methods for the synthesis of strong ground motion. In *Proceedings: Modeling Earthquake Ground Motion at Close Distances*, Palo Alto, CA, pp. 15–1 – 15–17. Research Project 3102-04, Electric Power Institute.

Hisada, Y., H. Bao, J. Bielak, O. Ghattas, and D. O'Hallaron (1998, December). Simulations of long-period ground motions during the 1995 Hyogo-Ken Nanbu (Kobe) earthquake using a 3-D finite element method. In *2nd International Symposium on Effect of Surface Geology on Seismic Motion*, Yokohama, Japan, pp. 59–66.

Huang, B., K. Chen, W. Huang, J. Wang, T. Chang, R. Hwang, H. Chiu, and C. Tsai (2000, September 1). Characteristics of strong ground motion across a thrust fault tip from the September 21, 1999, Chi-Chi, Taiwan earthquake. *Geophysical Research Letters 27*(17), 2729–2732.

ICBO (1997). *Uniform Building Code*. Whittier, CA: International Conference of Building Officials (ICBO).

Inoue, T. and T. Miyatake (1998, December). 3-D simulation of near-field strong ground motion based on dynamic modeling. *Bulletin of the Seismological Society of America 88*(6), 1445–1456.

Iwan, W. and X. Chen (1994). Important near-field ground motion data from the Landers earthquake. In *Proceedings of the 10th European Conference on Earthquake Engineering*, Volume 1, Vienna, pp. 229–234.

Ji, C., D. V. Helmberger, T. Song, K. Ma, and D. J. Wald (2001, December 1). Slip history and tectonic implication of the 1999 Chi-Chi earthquake. *Geophysical Research Letters 28*(23), 4379–4382.

Johnson, K., Y. Hsu, P. Segall, and S. Yu (2001, June 1). Fault geometry and slip distribution of the 1999 Chi-Chi, Taiwan earthquake imaged from inversion of GPS data. *Geophysical Research Letters 28*(11), 2285–2288.

Kamae, K. and K. Irikura (1998, April). Source model of the 1995 Hyogo-Ken Nanbu earthquake and simulation of near-source ground motion. *Bulletin of the Seismological Society of America 88*(2), 400–412.

Ma, K., T. Song, S. Lee, and H. Wu (2000, October 15). Spatial slip distribution of the September 20, 1999, Chi-Chi, Taiwan, earthquake (m(w)7.6) — Inverted from teleseismic data. *Geophysical Research Letters 27*(20), 3417–3420.

Ma, K., J. Wang, and D. Zhao (1996). Three-dimensional seismic velocity structure if the crust and uppermost mantle beneath Taiwan. *Journal of Physical Earth 44*(2), 85–105.

Ma, K.-F., J. Mori, S.-J. Lee, and S. Yu (2001). Spatial and temporal distribution of slip for the 1999 Chi-Chi, Taiwan, earthquake. *Bulletin of the Seismological Society of America 91*(5), 1069–1087.

Madariaga, R., K. Olsen, and R. Archuleta (1998, October). Modeling dynamic rupture in a 3-D earthquake fault model. *Bulletin of the Seismological Society of America 88*(5), 1182–1197.

Mai, P. and G. Beroza (2002, November 10). A spatial random-field model to characterize complexity in earthquake slip. *Journal of Geophysical Research - Solid Earth 107*(B11), 2308, doi:0.1029/2001JB000588.

Oglesby, D. D., R. J. Archuleta, and S. B. Nielsen (2000, June). The three-dimensional dynamics of dipping faults. *Bulletin of the Seismological Society of America 90*(3), 616–628.

Olsen, K. and R. Archuleta (1996, June). Three-dimensional simulation of earthquakes on the Los Angeles fault system. *Bulletin of the Seismological Society of America 86*(3), 575–596.

Olsen, K., R. Madariaga, and R. Archuleta (1997, October 31). Three-dimensional dynamic simulation of the 1992 Landers earthquake. *Science 278*, 834–839.

Olsen, K. B., R. J. Archuleta, and J. R. Matarese (1995, December 8). Three-dimensional simulation of a magnitude-7.75 earthquake on the San-Andreas Fault. *Science 270*(5242), 1628–1632.

Pitarka, A., K. Irikura, T. Iwata, and S. Sekiguchi (1998, April). Three-dimensional simulation of the near-fault ground motion for the 1995 Hyogo-ken Nanbu (Kobe), Japan, earthquake. *Bulletin of the Seismological Society of America 88*(2), 428–440.

Somerville, P. G., N. F. Smith, R. W. Graves, and N. A. Abrahamson (1997, January/February). Modification of empirical strong ground motion attenuation relations to include the amplitude and duration effects of rupture directivity. *Seismological Research Letters 68*(1), 199–222.

Wald, D. J., V. Quitoriano, T. H. Heaton, and H. Kanamori (1999, August). Relationships between peak ground acceleration, peak ground velocity and Modified Mercalli Intensity in California. *Earthquake Spectra 15*(3), 557–564.

Wells, D. and K. Coppersmith (1994, August). New empirical relationships among magnitude, rupture length, rupture width, rupture area, and surface displacement. *Bulletin of the Seismological Society of America 84*(4), 974–1002.

U.S. Geological Survey
525 South Wilson Ave.
Pasadena, CA 91106
(B.T.A.)

Department of Civil Engineering
Mail Stop 104-44
California Institute of Technology
Pasadena, CA 91125
(J.F.H.)

Department of Geologic and Planetary Sciences
Mail Stop 252-21
California Institute of Technology
Pasadena, CA 91125
(T.H.H.)